The geology and genesis of the iron skarns of the turgai belt, northwestern Kazakhstan

T. Hawkins, M.P. Smith, R.J. Herrington, V. Maslennikov, A.J. Boyce, T. Jeffries

PII: S0169-1368(15)30126-8
DOI: doi: 10.1016/j.oregeorev.2015.10.016
Reference: OREGEO 1646

To appear in: *Ore Geology Reviews*

Received date: 25 November 2014
Revised date: 16 July 2015
Accepted date: 13 October 2015

Please cite this article as: Hawkins, T., Smith, M.P., Herrington, R.J., Maslennikov, V., Boyce, A.J., Jeffries, T., The geology and genesis of the iron skarns of the turgai belt, northwestern Kazakhstan, *Ore Geology Reviews* (2015), doi: 10.1016/j.oregeorev.2015.10.016

THE GEOLOGY AND GENESIS OF THE IRON SKARNS OF THE TURGAI BELT, NORTHWESTERN KAZAKHSTAN.

T. Hawkins [1,2], M.P. Smith[1]*, R.J. Herrington[2], V. Maslennikov[3], A. J. Boyce[4], T. Jeffries[5].

1. School of Environment and Technology, University of Brighton, Brighton BN4 2GJ, UK.

2. Department of Earth Sciences, The Natural History Museum, London, SW7 5BD, U.K.

3. Institute of Mineralogy, Miass, Russia.

4. SUERC, East Kilbride, Glasgow, G75 0QF, Scotland, U.K.

5 Core Research Laboratories, The Natural History Museum, London, SW7 5BD, UK

*Corresponding author: martin.smith@brighton.ac.uk; Tel: +44(0)1273 642265

Abstract

The magnetite deposits of the Turgai belt (Kachar, Sarbai and Sokolov), in the Valerianovskoe zone of the southern Urals, Kazakhstan, contain a combined resource of over 3Gt of iron oxide ore. The deposits are hosted by carbonate sediments and volcaniclastic rocks of the Carboniferous Valerianovka Supergroup, and are spatially related to the gabbroic to granitoid composition intrusive rocks of the Sarbai-Sokolov intrusive series. The magnetite deposits are developed dominantly as metasomatic replacement of limestone, but also, to a lesser extent, of volcanic rocks. Pre-mineralisation metamorphism and alteration resulted in the formation of wollastonite and the silicification of limestone. Magnetite mineralisation is associated with the development of a high temperature skarn assemblage of diopside, grossular-andradite garnet, actinolite, epidote and apatite. Sub-economic copper-bearing sulphide mineralisation overprints the magnetite mineralisation and is associated with deposition of hydrothermal calcite and the formation of an extensive sodium alteration halo dominated by albite and scapolite. Chlorite formation accompanies this stage and further later stage hydrothermal overprints. The replacement has in places resulted in preservation of primary features of the limestone, including fossils and sedimentary structures in magnetite, skarn calc-silicates and sulphides.

Analysis of Re-Os isotopes in molybdenite indicates formation of the sulphide mineral assemblage at 336.2±1.3Ma, whilst U-Pb analyses of titanite from the skarn alteration assemblage suggests skarn alteration at 326.6±4.5Ma with re-equilibration of isotope systematics down to ~270Ma. Analyses of mineral assemblages, fluid inclusion microthermometry, O and S isotopes suggest initial mineralisation temperatures in excess of 600ºC from hypersaline brines (45-50wt. % NaCl eq.), with subsequent cooling and dilution of fluids to around 150ºC and 20wt. % NaCl eq. by the time of calcite deposition in late stage sulphide-bearing veins. $\delta^{18}O$ in magnetite (-1.5 to +3.5‰) and skarn forming silicates (+5 to

+9‰), $\delta^{18}O$ and $\delta^{13}C$ in limestone and skarn calcite ($\delta^{18}O$ +5.4 to +26.2‰; $\delta^{13}C$ -12.1 to +0.9‰) and $\delta^{34}S$ in sulphides (-3.3 to +6.6‰) and sulphates (+4.9 to +12.9‰) are all consistent with the interaction of a magmatic-equilibrated fluid with limestone, and a dominantly magmatic source for S. All these data imply skarn formation and mineralisation in a magmatic-hydrothermal system that maintained high salinity to relatively late stages resulting in the formation of the large Na-alteration halo. Despite the reported presence of evaporites in the area there is no evidence for evaporitic sulphur in the mineralising system.

These skarns show similarities to some members of the iron oxide-apatite and iron oxide-copper gold deposit classes and the model presented here may have implications for their genesis. The similarity in age between the Turgai deposits and the deposits of the Magnitogorsk zone in the western Urals suggest that they may be linked to similar magmatism, developed during post-orogenic collapse and extension following the continent-continent collision, which has resulted in the assembly of Laurussian terranes with the Uralide orogen and the Kazakh collage of the Altaids or Central Asian Orogenic Belt. This model is preferred to the model of simultaneous formation of very similar deposits in arc settings at either side of an open tract of oceanic crust forming part of the Uralian ocean.

Keywords: Skarn; Magnetite; Iron oxide-apatite; IOCG; Urals;

1. Introduction

The Kachar, Sokolov and Sarbai magnetite iron deposits are located in the north-west of Kazakhstan near the border with Russia, in a belt which extends into Russian territory (Fig. 1). These stratabound, massive, magnetite deposits contained at least 3000Mt of high grade iron ore (Fig. 2) and have been mined for more than 60 years. These deposits, together with other smaller satellite deposits and occurrences, form a long NNE-SSW trending magnetite rich belt, called the Turgai belt, which extends from the Sarbai deposit in the south to the Glubochensk deposit in the north (Fig. 3). The Turgai belt is hosted within the larger Valerianovka Arc, which is part of the larger Transuralian tectonic terrane that forms the eastern most edge of the Southern Uralides (Brown et al., 2006). The Uralides were formed during the collision of the Laurussia and Kazakhstan plates between the Carboniferous and Triassic (Brown et al., 2002; 2006).

Since their discovery by aeromagnetic geophysics in 1949 (Porotov et al., 1987) the massive magnetite skarns of the Turgai belt have been subject to several detailed studies (e.g. Smirnov and Dymkin, 1989; Sokolov and Grigor‘ev, 1977; Porotov et al., 1987; Zackarov et al., 1987; Bekmuhametov, 2004). These have revealed some distinctive characteristics that that are shared with a number of different deposit types. Most recently a number of workers have noted the similarities of these deposits to Kiruna-type deposits (Iron oxide-apatite or IOA) and related iron oxide-copper-gold (IOCG) deposits (Barton and Johnson, 1996; Herrington et al., 2002; Williams et al., 2005). Whilst the Turgai magnetite-rich ore deposits are predominantly carbonate-hosted skarns, the genesis and relative classification of the iron deposits of the IOA class in general is still a matter of controversy, with arguments favouring either direct magmatic crystallisation (e.g. Nyström, 1985), hydrothermal mineralisation involving magmatically derived fluids (e.g. Pollard, 2001), or hydrothermal mineralisation involving brines derived from interaction with evaporites (e.g. Barton and Johnson, 1996).

In this paper we review the available literature on the geology and mineralogy of the Turgai deposits, and present new geological, geochemical and isotopic observations of the ores. These are used to help constrain the formation of these deposits and to further develop a tectonic model for the formation of the Transuralian zone. These data are then compared with skarn, IOA and Iron oxide-copper-gold (IOCG) deposits worldwide to investigate implications for the development of this deposits class. The data are also compared with data from major skarn-type magnetite deposits in other tectonics zones of the Urals, notably at Magnitogorsk and Mali Kuibas (Herrington et al., 2002), to provide constraints on the tectonic setting of major iron skarn development, and to provide further understanding of the genetic relationships to other deposit types.

2. Local Geology

The Turgai deposits are hosted within the volcanic and sedimentary rocks of the Transuralian zone. The Uralides are a 2500 km long, north-south trending mountain belt that extend from northern Kazakhstan to the Arctic Ocean, and were formed as a result of the collision of the Laurussia and the Siberia-Kazakh plates during a period spanning the Late Carboniferous to Early Permian. On a regional scale, the Southern Uralides can be divided into geologically distinct sub-zones, bounded by large, north-south trending structures (Fig. 1). The Transuralian zone is bounded in the west by the Troitsk fault and the Kartaly Reflection Zone (Brown et al. 2002) and in the east by the older rocks of the Kazakh collage. This zone is poorly exposed and comprises a Lower Palaeozoic basement overlain by rocks of the Irgizkaya, Alexandrovskaya and Valerianovka arcs which are composed of Devonian and Carboniferous calc-alkaline volcano-plutonic complexes, overlain by terrigenous red beds and evaporites (Herrington et al., 2005a).

The Valerianovka arc (or Valerianovskoe zone) is host to the key deposits discussed in this paper (Fig. 3). The arc is an approximately 1000km long belt of interbedded Silurian to Carboniferous sediments, volcanic rocks and granitic intrusions (Zonenshain, 1984). It is bounded in the west by the Livanovsk fault and in the east by the Anapovsk fault. It is covered by a thick layer of Mesozoic sediments which include extensive sedimentary iron ores, but can be traced northeast – southwest along strike by its highly anomalous magnetic signature. Herrington et al. (2005b) proposed that the zone extends southwards beneath the sedimentary cover and may correlate with the Middle Tien Shan arc which hosts the Almalyk porphyry copper-gold deposit in Uzbekistan. The Valerianovka arc is host to a number of significant porphyry copper prospects, including Benkala (Herrington et al., 2005a)

The Carboniferous sequence that hosts the giant iron ore deposits of the Valerianovka arc is more than 3.5 km thick (Bekmuhametov, 2004) and its stratigraphy is summarised in Figure 4. In the Valerianovka arc, early, rift-related sedimentary rock sequences are overlain by two volcano-sedimentary successions, the Valerianovka and Kachar Supergroups (Bekmuhametov, 2004). The western boundary region of the megazone hosts the Karashtau, Djhabyk-Karagandski and Milutin intrusive formations as well as the Irgiz formation in the far south. The central region hosts the iron-bearing volcanic sediments and limestones of the Valerianovka supergroup. These units are intruded by bodies of the Sarbai-Sokolov intrusive series in the north and by the gabbro-granites of the Sulukul complex in the south. The Eastern boundary zone is comprised of undifferentiated volcanic rocks and limestones and Devonian volcanic rocks which host the granodiorite Ubagan complex. The entire region has been faulted by NNE-SSW trending faults. The Sarbai-Sokolov intrusive suite is important in an account of the geology of the ores as intrusions of this group are most closely associated with the Turgai ores, and occur within the Kachar open pit in contact with magnetite skarn. The suite is composed of an apparently linked suite of gabbro – diorite - quartz-diorite –

granodiorite (Ksenofontov and Ivlev, 1971). According to Ksenofontov and Ivlev (1971) all these rocks contain model biotite, up to 10% of the rock in the case of the most evolved examples. In the South of the Valerianovka arc the lined Adaevka and Benkala intrusive bodies are composed of the more felsic quartz diorites and granodiorites (Ksenofontov and Ivlev, 1971) and host porphyry style mineralisation.

The Valerianovka Supergroup comprises more than 1000m of andesite lavas and volcaniclastic sediments, overlain by siliciclastic and carbonate rocks. Carbonate rocks and sandstones of the Valerianovka Supergroup were deposited in a shallow marine environment during the Tournaisian. Anhydrite layers and mudstones are recorded within limestones in the upper part of the supergroup. This was followed by an intense period of volcanism that started in the middle Visean with three defined peaks in the middle Visean, the late Visean and the Serpukhovian. These produced the volcanic sequences of the Sarbai, Kurzunkhul and Andreevka suites within the Valerianovka and Kachar Supergroups (Zackarov et al., 1987). Basaltic-andesite and andesite dominate the pile, which has been interpreted as representing a single, large-scale, continental volcanic event (Samarkin and Pumpyanskiy, 1983). Directly overlying the Valerianovka Supergroup, the Kachar Supergroup is a ~800 m thick unit of conglomerates, tuffs and sediments interbedded with mafic to intermediate flows and their pyroclastic equivalents, interpreted to be largely subaerial in origin (Pumpyanskiy et al., 1985). This sequence is intruded by gabbros and diorites of the Sarbai-Sokolov complex, considered to be co-magmatic with the Kachar Supergroup volcanic rocks (Ksenofontov and Ivlev, 1971) and as such, part of the Valerianovka volcano-plutonic complex. The Sarbai-Sokolov volcanic-plutonic complex and associated magnetite deposits were formed as a result of igneous activity from the Visean to the Serpukhovian. Conglomerates, sandstones, and calcareous siltstones were accumulated in depressions in the late Palaeozoic; they were accompanied by periodic basalt lava flows.

A group of associated series of igneous rocks were intruded into the Transuralian Zone, including parts of the Valerianovka arc: the Sarbai-Sokolov, Ubagan, Milutin, Djhabyk-Karagandski and Pridorogny Series. The Ubagan series is dominantly granodiorite in composition. The Sarbai-Sokolov series was intruded from 345-322Ma (Fershtater et al., 2007) and consists of diorite and quartz diorite stocks, dikes and gabbro-diorite massifs. The Milutin series consists of a group intrusions ranging in composition from gabbroic to biotite granites. These were intruded from 342-310Ma (Ronkin, 1989) and may be related to the volcanic units of the Kachar Supergroup. Dykes of comparable composition and age also cross-cut the ore at Sarbai. The Djhabyk-Karagandski (296-276Ma; Ksenofontov and Ivlev, 1971) and Pridorogny Series' (Permian) are post-orogenic 2 mica granites and leucogranites that post-date the iron mineralisation in Transuralian zone.

3. Deposits

The Valerianovka arc rocks host the giant, and currently producing, Sarbai, Kachar and Sokolov iron deposits along with many prospects, such as Glubochensk, in a district known collectively as the 'Turgai belt' (Bekmuhametov, 2004). Sarbai, Kachar and Sokolov together represent over 3 billion tonnes of iron ore, comparable in scale to some of the largest hydrothermal iron oxide-apatite deposits, notably the Kirunavaara deposit, Sweden (Fig. 2). The Sarbai and Sokolov deposits are located near the town of Rudny, whilst the Kachar deposit is located 5km to the north-west.

The Sokolov deposit had quoted reserves + resources in 1970 of 967 Mt at a grade of 41% Fe, with 0.07 to 0.11% P (Sokolov and Grigor'ev, 1977). The most recent estimate of remaining proved resources for Sokolov is 11.4Mt at a grade of 32% Fe, accessible via underground mining (ENRC, 2013). The current open pit is approximately 1 km wide at its

narrowest and 2.3 km long in a North-South direction. Most of the iron ore is found in a series of 5 stacked, stratabound, magnetite lenses distributed over a strike length of 5.6 km, stratigraphic thickness of 500 m, and extending down a 50°E dip for approximately 1 km, surrounded by large envelopes of disseminated magnetite (Fig. 5a). The orientation changes to a westerly dip towards the southern end of the deposit. Sokolov is located on the eastern limb of a NNE-trending anticline that hosts the Sarbai deposit on its western limb. The geological setting and succession within the host Early Carboniferous Valerianovka Supergroup at Sokolov is broadly similar to that described by Herrington et al. (2005a). The host sequence comprises a lower 1500 m of porphyritic andesites, volcanic breccias and tuffs, overlain by 800 m of limestone, micro-porphyritic basalts and associated tuffs, and calcareous tuffs, capped by 1500 m of porphyritic andesite-basalts, tuffs and tuff-breccias. The upper part of the sequence was eroded and overlain by Upper Palaeozoic red-beds, prior to tilting, and subsequently masked by 50 to 120 m of Mesozoic-Cenozoic sediments (Sokolov and Grigor‘ev 1977). The deposit is hosted within carbonate rocks, lesser intercalated tuffaceous sediments, and intermediate volcanic rocks in the middle unit of the Valerianovka Supergroup (Fig. 4). The host sequence is intruded by the northeast elongated, 15 x 3.5 km intrusive mass of the Sarbai-Sokolov gabbro-diorite-granodiorite suite (Fig. 5a). This suite is bounded by a series of NNE trending faults and cross cut by albitised granites and diabase microporphyrites. In parts of the deposit, there are also sill-like and discordant bodies of pre- to post-ore porphyritic dolerite, plagiogranites and diorite porphyries (Sokolov and Grigor‘ev 1977). The magnetite ore lenses are generally conformable to the host rock bedding and volcanic contacts throughout the deposit, although there are some local discordancies (Smirnov and Dymkin, 1989; Figs. 5a; 6b; 7a, b). Alongside magnetite there are significant accessory apatite and sulphides, mainly pyrite, pyrrhotite and chalcopyrite. Thin sulphide layers are formed in the footwall of the magnetite bodies, with the highest

concentrations in the central portions of the deposit. Overall the sulphur content of the ores varies from 2.4 to 3.3% (Sokolov and Grigor'ev, 1977). Extensive scapolite alteration occurs on the margins of the mineralisation and forms a hanging-wall blanket to the ore (Fig. 6b). Skarn alteration of calcareous rocks is dominated by garnet and diopside, with lesser albite, chlorite, actinolite, epidote and calcite alteration. The development of calc-silicate alteration is less volumetrically extensive than magnetite alteration, and mainly developed on the margins of the magnetite ore bodies. The magnetite ore has also been oxidised to hematite, in some places with a martite texture.

The Sarbai deposit lies approximately 8 km northwest of the Sokolov deposit on the western limb of the NNE-trending Sokolov-Sarbai anticline (Fig. 3). It had original combined reserves and resources of 725 Mt of ore at a grade of 45.6% Fe, 4.05% S and 0.13% P (Sokolov and Grigor'ev, 1977). The most recent remaining combined open pit resource for Sarbai is 61.3Mt at 37% Fe, with a further 3.3Mt at 31.4%Fe available for underground mining (ENRC, 2013). The current open pit is approximately 1.7km wide at its narrowest and 2.4 km long in a north-south direction. The geological setting at Sarbai is similar to that of the Sokolov deposit (Figs. 5b; 6a; 7c). The mineralisation replaced a 350-400m thick succession of bituminous limestones and intercalated calcareous tuffs and tuffaceous sedimentary rocks of the Valerianovka Supergroup (Chuguevskaya 1969). The ore layers are conformable and appear to be bedded, passing laterally into less altered tuffaceous units and calcareous sedimentary rocks. The Sarbai magnetite ore bodies are at no point in direct contact with the diorite of the Sarbai-Sokolov suite. At Sarbai, the intrusive complex comprises pyroxene and quartz-diorites and diorite porphyries accompanied by various pre-, intra- and post-ore dyke phases, culminating in post-ore quartz-pyroxene and granite porphyries (Dymkin 1966). The deposit is also cut by late, post-ore rhyolite to rhyodacite dykes that clearly cross-cut mineralisation (Fig. 6b; Fig. 7d). Pre-ore diorite porphyry dykes

follow generally north-south trending faults which dip at 65 to 70°W. Post-ore structures displace and brecciate the ore and country rock and control the orientation of post-ore granite-porphyry dykes (Sokolov and Grigor‘ev, 1977).

The Sarbai deposit consists of three main, generally north-south trending ore lenses, approximately concordant to the host fabric. These lenses measure approximately 1000 to 1700 m long, 800 to 1700 m wide laterally and are 170 to 185 m thick. The western ore zone consists of two ore layers, separated by epidotised and amphibolitised host rock. The dominant ore mineral is magnetite, accompanied by significant accessory sulphides, mainly pyrite, pyrrhotite and chalcopyrite, responsible for contents of between 2.5 and 3.3% S in the bulk ore (Sokolov and Grigor‘ev 1977). The banded nature of both the massive and disseminated magnetite ores is assumed to have been inherited from the sedimentary and volcano-sedimentary host rock that it has replaced. Pre-ore hornfelsing accompanied contact metamorphism, most clearly developed in limestone, and including the development of wollastonite. Alteration comprises the subsequent development of biotite-K feldspar and sodic alteration assemblages in the enclosing silicate hosts, and pyroxene-garnet, pyroxene-scapolite and epidote-actinolite assemblages directly associated with the ore formation in the carbonate dominated hosts. Scapolite is most significantly developed as part of the sodic alteration assemblage in silicate host rocks, but can occur alongside the more typical skarn calc-silicates within limestone replacement. Post-ore alteration comprises chlorite-prehnite, calcite-silica and zeolite (Sokolov and Grigor‘ev, 1977). Alteration has been reported to be zoned outward from the main Sarbai-Sokolov intrusive (Sokolov and Grigor‘ev, 1977): (1) biotite-albite-scapolite in volcanic hosts, (2) garnet-pyroxene skarn in the footwall of the magnetite ore, (3) 'skarn' ore (dominantly magnetite and scapolite) in the carbonate hosts, (4) scapolite-pyroxene alteration, (5) pyroxene skarns in the hanging wall passing out into hornfels, (6) calcic amphiboles associated with hornfelsing and albitised volcanic country

rocks. From our observations the alteration within magnetite skarn is dominated by epidote, garnet and pyroxene, with scapolite mainly occurring in the altered host volcanic rocks distal to the main magnetite zone.

The Kachar deposit is the largest in the Turgai belt, with published original ore reserves and resources of 1 Gt averaging 44.9% Fe, between 0.5 and 3% S and 0.15 to 0.33% P (Sokolov and Grigor‘ev 1977). Remaining proved resources were estimated as 130Mt at a grade of 37.8% Fe (ENRC, 2013). Sulphides are common accessories throughout the mineralised zone, although present at a lower concentration compared to the other deposits of the belt. The Kachar deposit is again hosted by the Valerianovka Supergroup, here comprising andesitic porphyries, pyroclastics with intercalated tuffs and limestones, marls with lenses of anhydrite near the magnetite orebodies, basalt and dacite lava flows, and pyroxene-plagioclase porphyries and their tuffs at the top (Fig. 5c; 6c). The overlying Kachar Supergroup locally comprises up to 800 m of polymict tuffaceous sandstones, conglomerates, argillites, porphyritic andesite tuffs, basalt and andesite flows, and plagioclase and pyroxene-plagioclase porphyries and tuffs. The volcano-sedimentary sequence surrounding the deposit is cut by numerous small stock-like and irregular, quartz-bearing granitoid-porphyry intrusive rocks which have been strongly albitised and scapolitised. The deposit is divided into six separate fault bounded blocks distinguished by lithology, morphology and attitude of their folds, intensity of fractures and shape of the ore bodies (Porotov et al. 1987). Four of the blocks comprise of a sequence of interlayered volcanic and sedimentary rocks, whilst the remainder are composed of unstratified volcanic rocks and have been interpreted to have formed in the vent of a palaeo-volcano (Porotov et al., 1987).

The Kachar iron ore zone comprises a series of stacked, stratabound, massive magnetite lenses, separated and surrounded by lower grade segregated magnetite-scapolite, with a bulk grade of up to 70% magnetite (Fig. 5c; 6a). The individual massive magnetite

lenses, which have dimensions of as much as 1 x 1 km and up to 100 m in thickness, are composed of fine to coarse grained, euhedral, massive magnetite. The ore is developed in both volcanic rock and limestone protoliths (Figs. 5 and 6), but the preservation of limestone structures, and in particular fossils, strongly suggests that the majority replaced limestone. The ore is closely associated with extensive zones of scapolite and albite alteration, in addition to other phases. Extensive scapolite alteration largely in volcanic protoliths, with associated pyroxene, post-dates all of the intrusive phases cutting the Valerianovka Supergroup in the immediate deposit area, and in places is associated with massive magnetite. Other alteration minerals include actinolite, tourmaline, apatite, chlorite, albite, zeolite and calcite. In places, close to magnetite mineralisation, alteration may comprise pyroxene (diopside)-albite or pyroxene-garnet (andradite).

Anhydrite has been reported as bodies within both the limestone and massive magnetite, and as 'nests' and pseudomorphs after feldspars and quartz in the pre-mineralisation intrusive granitoid porphyries that are common in the magnetite ores. The anhydrite-bearing layers reported by Porotov (1987) are between 40-100m thickness and compose the lower part of the Sokolov suite. Stratiform chalcocite and bornite have been found associated with anhydrite in these rocks. This unit has been variously interpreted to be hematite-silica-anhydrite hydrothermal alteration of clastic and pyroclastic material (Porotov et al. 1987) or as evaporite layers within the limestone (Belyashov and Plekhova, 1965). These beds are not exposed in the current accessible mining and no drillcore of this material was located during the course of this study. Nodular facies have been observed in the limestone during this study, which may be consistent with the development of sabkha like environments during the periodic dessication of the predominant reef and lagoonal facies within the limestone sequence.

4. Methods

5.1 Electron microscopy and probe analyses.

Back scattered electron (BSE) images of the microscopic features of the samples were taken using a JEOL 5900 V Scanning Electron Microscope (SEM) and mineral analyses were made using a Cameca SX100 electron microprobe. Scanning electron microscopy was carried out at 20kV accelerating voltage and 2nA beam current. Energy dispersive spectra were acquired using an Oxford Instruments INCA X-sight Si (Li) energy dispersive X-ray micro-analyser, and data analysed using the INCA software. For electron microprobe analyses beam conditions were set at 20Kv and 20nA with a spot size of 1μm. The instrument was calibrated using well characterised silicate, sulphide, halide and oxide mineral standards for Na, Mg, Si, S, Cl, Ca, Ti, Fe, and Sr, synthetic ScPO4 and KBr for P and K respectively, and pure metals for Cr, Mn, Co, Ni and Cu. The data was empirically corrected for peak overlaps using analyses of standards following the techniques outlined in Willams (1996).

5.2 Re-Os dating of molybdenite

One sample of molybdenite-bearing rock was processed for molybdenite separation following the methods presented by Selby and Creaser (2004), using metal-free crushing, gravity, magnetic and water-floatation methods. A pure mineral separate of molybdenite could not be obtained as a result of the intergrown magnetite, and the analyzed fraction contained >50% epidote and magnetite impurities. Magnetite may host significant Re and Os (e.g. Mathur et al.,2002) and so some caution must be exercised with the model ages as presented. However, the fact that 2 separate analysese were repeatable within error suggests that epidote and magnetite contained negligible osmium in this case. The ^{187}Re and ^{187}Os concentrations in the

molybdenite-bearing separate were determined by isotope dilution mass spectrometry at the University of Alberta Radiogenic Isotope Facility following the methodology of Selby and Creaser (2001, 2004) using a Thermo Scientific Triton mass spectrometer.

5.3 U-Pb Laser ablation ICP-MS dating of titanite.

Analyses of the U-Pb isotopic ratios of titanite from the central pit of Sokolov deposit were completed at the Natural History Museum, London, following the methods outlined in Storey et al. (2006). Polished blocks of the skarn containing titanite were prepared using diamond paste. The blocks were scrubbed by hand in deionised water before 1 minute in an ultrasonic bath to remove impurities. Samples were ablated with a New-Wave UP213 Frequency quintupled Nd:YAG laser (213nm-UV) with a 30μm laser spot size connected to an ICP-MS – ThermoElemental PlasmaQuad III and carried using He gas. Detailed analytical conditions are given in Storey et al. (2006). The stable ^{204}Pb isotope composition within the sample was measured for accurate common Pb corrected age data. Significant compositional overlaps using this technique between Hg and ^{204}Pb require 70% of the Hg to be stripped from the Ar (neb) and He (carrier) gas by Au-traps. The Hg stripped signal and the IUPAC natural atomic abundance ratio of 0.521 was used to determine the common lead concentration. Most analyses of titanite showed evidence for surface contamination (a dip in count rate was observed in the time resolved spectra as the surface layer was ablated through) and so only the latter parts of the signal were integrated for age determination. The common lead correction of the data was carried out using the procedure outlined in Storey et al. (2006) using the analytically determined ^{204}Pb composition of the samples and the Stacey and Kramers (1975) model terrestrial ^{208}Pb/^{206}Pb ratio. Data were analysed using the ISOPLOT program (Ludwig, 2003).

5.4 Fluid inclusion microthermometry

Microthermometric analysis of fluid inclusions was carried out using a LINKAM TMS600 heating freezing stage mounted on a Nikon Eclipse 600 petrological microscope. The stage was calibrated using synthetic water-CO_2 fluid inclusions, distilled water and a range of pure solids. Measurements were made at a heating rate of 0.5°C/min below 0°C, and 5°C/min during heating to 600°C. Precision is estimated from repeated analyses of inclusions as ±0.1°C for melting temperature measurements, and ±2°C for halite dissolution and homogenisation temperature measurements. The salinity of fluid inclusions as weight % NaCl equivalent (wt. % NaCl eq.) was calculated using the equation of Bodnar (1993) for ice melting, and the equation of Sterner et al. (1988) for halite dissolution. Other cations are almost certainly present, but hydrohalite (in L+V inclusions) and ice melting (in L+V+Sh inclusion) which would have allowed estimation of bulk salinity and major cation ratios in systems such as NaCl-$CaCl_2$-H_2O, were not observed. The salinities are thus minimum salinities, but allow comparison with wt. % NaCl eq. data from other deposits. Isochores were calculated using the ISOC program of Bakker (2003).

5.5 Stable isotope analyses.

Samples of magnetite, hematite, garnet, pyroxene, epidote, sulphide and sulphate minerals were handpicked and microdrilled from hand specimen. These separates were then powdered in an agate mortar. For oxygen isotope analyses of silicates and oxides approximately 1-3 mg of powdered sample was fluorinated to release O_2 using ClF_3 and a CO_2 laser fluorination system (Sharp, 1990). Oxygen isotope analyses of carbonate minerals were undertaken on

approximately 10mg sample separates together with the analyses of carbon isotopes following the conventional methods of McCrea (1950) and Rosenbaum and Sheppard (1986). Oxygen isotope ($\delta^{18}O$) values are reported in the standard per mil notation relative to the Vienna Standard Mean Ocean Water (V- SMOW). Carbon isotope analyses are expressed as per mil (‰) deviations relative to the Vienna Peedee Formation Belemnite (V-PDB) standard.

Sulfides were analysed by standard techniques (Robinson and Kusakabe, 1975) in which SO_2 gas was liberated by combusting the sulfides with excess Cu_2O at 1075°C, *in vacuo*. Liberated gases were analysed on a VG Isotech SIRA II mass spectrometer, and standard corrections applied to raw $\delta^{66}SO_2$ values to produce true $\delta^{34}S$. The standards employed were the international standards NBS-123 and IAEA-S-3, and the SUERC standard CP-1. Repeat analyses of these standards gave $\delta^{34}S$ values of +17.1‰, -31.5‰ and -4.6‰ respectively, with a standard error around ±0.2‰. Data are reported in $\delta^{34}S$ notation as per mil (‰) variations from the Vienna Cañon Diablo Troilite (V-CDT) standard.

5. Results

6.1 Alteration and Mineralisation

A simplified and generalised paragenesis of the deposits is presented in Figure 8. Mineralisation is developed replacing limestone and volcaniclastic rocks, both of which preserve well defined primary features away from the main ore zones (Fig. 9a, b). Macro-scale field relations (Fig. 7) where magnetite can clearly be seen to be developed along limestone bedding, previous mapping (Figs. 5 and 6) and the occurrence of clear limestone replacement textures, all indicate that magnetite ore was dominantly developed in limestone,

with subsidiary amounts of ore developed replacing the volcanic rocks. The development of the mineralisation in the main limestone-hosted ore zone can be summarised by the following stages (Fig. 8):

A pre-ore phase: This is characterised by silicification, formation of calc-silicates and contact metamorphism of the limestone host rock. Wollastonite, calcic-amphiboles, calcic-pyroxenes, apatite and quartz are associated with the pre-ore phase of alteration. Textures include fine grained, euhedral pyroxenes developed within the limestone as well as subhedral wollastonite and very fine quartz, which has locally preserved primary features of the host rock (Fig. 10a). Minerals are disseminated with no local spatial associations with veins. This alteration is rarely seen in the centre of the deposit where it has been overprinted by subsequent phases. Where the pre-ore phase has been overprinted by subsequent alteration, euhedral apatite and calc-silicates are distinguished from those developed during later phases by distinct corroded edges. At the periphery of the deposits this alteration is clearly seen and is overprinted by post-ore sodic alteration forming albite and scapolite.

An Ore phase, which can be further subdivided into;

(a) *The skarn stage*, replacing limestone: typically containing calc- and alumino-silicates, massive iron oxide ore and minor iron-rich sulphides. The great bulk of the magnetite ore was formed during the skarn alteration and replacement of the limestone or volcanic host rock. This phase of alteration is characterised by epidote, calcic-pyroxenes (dominantly diopside – see below), calcic-garnets, calcic-amphiboles (tremolite and actinolite), magnetite, calcite, and pyrite with minor titanite and apatite (Fig. 8b-f). The mineral assemblage varies with the distance from the centre of the deposits. The main skarn mineral assemblages include epidote-titanite-magnetite, pyroxene-garnet-magnetite, epidote-pyroxene-magnetite, epidote-diopside magnetite and diopside-magnetite. Magnetite is intergrown with all the calc-silciate

phases, but also cross-cuts them in thin veins (Fig. 10b). This late phase magnetite is often massive and coarse grained. At the Sarbai and Sokolov deposits late magnetite breccias contain clasts of skarnified host rock (epidote + pyroxene) in a matrix of up to 60% coarse grained magnetite matrix. At the Kachar deposit several phases of magnetite and pyroxene formation are indicated from the coarse grained veins that cross cut the massive ore zones. These veins contain up to 9cm long, euhedral, diopside crystals in a coarse grained magnetite matrix.

(b) *The sulphide stage*: The main skarn alteration is overprinted by a distinct phase characterised by massive zones of sulphide in the core of deposits and sulphide-rich calcite veins associated with extensive sodic and potassic alteration. These veins contain sparry, white calcite, albite, magnetite and minor quartz, and carry sulphides, including pyrite, chalcopyrite, pyrrhotite, sphalerite, galena, molybdenite and arsenopyrite (Fig. 11a-d). Sulphides associated with this stage are often very fine and occluded within other gangue and sulphide minerals. In addition to calcite, albite, K-feldspar and minor quartz, the gangue mineralogy includes scapolite and chlorite. Sulphide-rich alteration zones can contain up to 10% each of chalcopyrite and pyrite, as both large clots of fine grained anhedral minerals and in coarse calcite veins. One characteristic texture found at all deposits was round blebs of sulphide minerals, 10 to 50 μm in diameter, occluded by either euhedral magnetite or by pyrite (Fig. 11e). In reflected light it can be seen that pyrite occurs overgrowing magnetite, sometimes associated with other sulphides (Fig. 12 a, b). Where hematite also occurs it is typically replacing magnetite and not assicated with the sulphide assemblage (Fig. 12c). Even where hematite occurs as the dominant Fe oxide at hand specimen scale, it is always associated with relict magnetite at the microscale (Fig. 12d). Pyrrhotite is less extensively developed, but occurs alongside pyrite and chalcopyrite (Fig. 11a), and occasionally in massive pods associated with pyrite (Fig. 11b). Pyrite and pyrrhotite do not occur directly

intergrown, but do occur adjacent to one another at the junction of massive pods (Fig. 12e) alongside magnetite, and pyrite occurs as micro-inclusions in pyrrhotite and vice versa (Fig. 12 e, f) suggesting they may have co-precipitated. There was clearly an alternation between pyrite and pyrrhotite deposition, as euhedral pyrite occurs within fractures in pyrrhotite, alongside magnetite (Fig. 12g) and chalcopyrite (Fig. 12h). This is in contrast to some IOCG systems where pyrrhotite is a late overprint on pyrite (Barton, 2014). Sphalerite is rare, but when present, is commonly associated with galena and chalcopyrite as very fine blebs within late stage pyrite. The latest sulphide deposition occurs as galena in very fine veinlets that cross cut other sulphides, and in very late calcite veins (Fig. 11c). The sulphide phase of alteration is found predominantly in the centre of the deposits, overprinting the skarn phase. Within these zones, the major gangue phase is coarse, euhedral calcite, although albite and K-feldspar (Fig. 11f) are also found as accessory minerals both within the calcite veins and as part of the selvage assemblage.

(c) *The chlorite stage*: This consists of coarse grained, sparry calcite veins that host coarse euhedral magnetite and coarse specular hematite. Characteristic chlorite- and calcite-rich alteration halos surrounding these veins have associated blocky magnetite, and can contain up to 30% chlorite.

Where there is weathering of massive magnetite ore, magnetite is hematised forming a martite texture. In places chalcopyrite has been altered to Cu-silicates and cuprite, pyrite to goethite and alteration rims of greenockite (CdS) are found with sphalerite. Other late-stage minerals include coarse gypsum in veins. This late alteration of the sulphides is commonly associated with barite and chlorite and is not volumetrically significant. At the Sarbai and Sokolov deposits, late silver-bearing phases include silver tellurides and native silver, and cross cut the minerals of the late sulphide phase.

Post-ore phase: distinguished by coarse, cross-cutting veins containing varying amounts of calcite, K feldspar and albite. They cross cut all other alteration and mineralisation and are distinct in that they lack any ore metals. This phase of alteration may, or may not be, associated with the widespread alteration that surrounds the deposits, extending for hundreds of metres into the host rock, which is characterised by coarse euhedral scapolite and albite porphyroblasts, and by quartz-replacement of the host limestone (Fig. 13a). The development of sparse gypsum veins cross-cutting earlier mineralisation also occurred at a later stage (Fig. 11g).

Distal alteration of the host rock. A characteristic feature of the magnetite skarns of the Turgai belt is the large scale sodic alteration that has affected the host rock for hundreds of metres around the limit of the deposits. This is visible at the field scale with the development of scapolite within andesitic volcanic rocks (Fig. 13a) in the matrix to magnetite-altered volcanic breccias (Fig. 13b, c), and at the microscale, where in the volcanic rocks albite and scapolite are formed from the sodic alteration of pre-existing primary feldspars (Fig. 13d, e). The distal alteration of the limestone host is mineralogically very similar to that of the volcanic host, but in this case albite and scapolite form euhedral porphyroblasts (Fig. 13f). The occurrence of limited amounts of scapolite in the main ore zone, and the intergrowth of scapolite with calc-silicates and magnetite in the volcanic rocks indicates this may be an additional alteration facies associated with the main ore stage.

The Kachar deposit is the largest of the three deposits and shows most departures from the generalised paragenesis given above. The centre of the deposit is formed of massive magnetite with disseminated pyrite and minor chalcopyrite throughout. Trace amounts of disseminated scheelite have also been found in the massive magnetite ore. Fine pyrite stringers associated with chlorite cross-cut the magnetite mineralisation. Cross-cutting calcite veins are sometimes lined with selvages of hematite-altered magnetite and in places

associated with coarse grained assemblages of intergrown hematite, magnetite and calcite. These veins are associated with the late chloritisation of the host rock. The ore zone lies adjacent to a 20m thick zone of veined marble that contains no magnetite, with ~10cm diameter vugs lined with fine-grained, euhedral pyrite and coarse-grained euhedral calcite.

6.2 Replacement textures

In general, alteration has obliterated primary rock textures at the centre of the deposits. However, there are locations where very fine scale host rock textures are preserved by skarn minerals. The preservation of the features of the host rock generally increases with distance from the central magnetite ore zone. Where there is pseudomorphism within the central ore zone the fine features of fossiliferous limestones are preserved by pyrite and pyroxene within a coarse magnetite matrix. Examples of excellent preservation textures include pyrite and magnetite replacement of primary limestone lamination (Fig. 14a), pyroxene, magnetite and pyrite after bivalves (Fig. 14b, c, d), chalcopyrite after goniatites (Fig. 14e), and pyroxene after coral (Fig. 14f), all of which are in a magnetite matrix. A characteristic feature of the Sokolov, Sarbai and Kachar deposits is that their ore zones are formed of bedding concordant magnetite lenses. The ore lenses often contain 5cm thick alternating layers of magnetite and pyrite that are likely to be ghost textures after limestone bedding and lamination these layers dip and strike in the same direction as the beds of the unaltered host rocks. This banding of the rocks, common in all of the deposits, is continuous laterally and in places these layers grade into altered host rock. These textures clearly indicate a significant portion of the magnetite ore was developed by limestone replacement.

6.3 Mineral chemistry

Mineral chemistry determined by electron microprobe is summarised in Table 1 and Figure 15. Clinopyroxene compositions from all the deposits are intermediate between diopside ($CaMgSi_2O_6$) and hedenbergite ($CaFeSi_2O_6$) although in general they are magnesium-rich (Fig. 15a). They exhibit low concentrations of Al and low but measurable Ti, Mn, and Na concentrations with no detectable K. All of the iron is assumed to be Fe^{2+}. Garnets from the Sarbai and Sokolov deposits are consistently calcium-rich and have an intermediate composition between grossular ($Ca_3Al_2Si_3O_{12}$) and andradite ($Ca_3(Fe^{3+},Ti)_2Si_3O_{12}$) (Fig. 15b). Analyses of Sarbai and Sokolov feldspars indicate that they are Ca-poor, and either very K or Na rich. Coexistence of albite and non-perthitic K-feldspar is common in distal skarn and reflects low miscibility of alkali feldspar end-members under skarn-forming conditions (Lowell and Noll, 2001). The variability of the amphibole chemistry was limited in general to the concentration of calcium, magnesium and iron with only minor variations in other elements. Identification of the amphiboles was mainly by chemical composition as these minerals were poorly crystalline and very fine grained. The most likely end members of these amphiboles are actinolite, ferroactinolite and tremolite (Fig. 15d). Early and distal alteration of the limestone formed calcic, magnesian, fine-grained amphiboles. Amphiboles associated with the main skarn phase have a more iron rich composition in general, however magnesian-amphiboles are often intergrown with ferroan-amphiboles. Scapolite was found at all three deposits. The scapolite is consistently Cl rich with variations of between 1.83 and 3.91 wt. % (Fig. 15e). The lack of a consistent correlation between the Cl-content of scapolite and the Ca-content is probably a result of the partial replacement of pre-existing Ca-plagioclase. Magnetite found in the central ore zones of all three deposit contains variable but low concentrations of TiO_2 (up to 1.42%, with an average of 0.15%) and consistently very low concentrations of MgO, MnO and Cr_2O_3. Two

samples collected from the distal alteration zone of the Kachar deposit, within the volcanic host rock contained appreciable quantities of TiO_2. Analyses of calcite in veins show that there are very low concentrations of both Fe and Mg compared with calcite in the altered limestone (Table 3; Fig. 15c). The most Mg enriched calcite is found in the matrix of the altered limestone intergrown with calcic-ferroan and -magnesian amphiboles.

Chlorite was analysed from all three deposits, and is typically Fe-rich (Fe/Fe+Mg atomic ratio <0.5) with Si ranging from 5.5 to 8.0 a.p.f.u. (Table 2; Fig. 15f). The tetrahedral site aluminium occupancy (Al(IV)) from 10 samples was used to establish the temperatures of chlorite formation using the technique of Cathelineau (1988). The data define a high T group from ~250-350°C, consistent with the late stages of skarn alteration, whilst the majority of the data fall in the range 60-180°C, probably consistent with a late overprint on the ore (Fig. 15g). The data should be viewed with caution however, because some chlorite compositions fall outside the range of the original study, and because of some possible issues with the theoretical validity of the technique (De Caritat et al., 1991). A range of chlorite geothermometry techniques have been developed which may give inconsistent results and so these data can only be regarded as giving an indicative relative range of chlorite formation temperatures.

6.4 Age of ore and alteration

The results of radio-isotope analyses are presented in Tables 4 and 5 and Figure 16. Molybdenite was found in two samples from the Sarbai deposit and from petrographic studies it can be seen that it clearly cross cuts the minerals of the main skarn phase, and is therefore paragenetically later and thus might give a minimum age for the mineralisation. The molybdenite is intergrown with allanite and epidote in places. The age determined from the

molybdenite from the Sarbai deposit is 336.2 ± 1.3 Ma. The age was reproduced within error by a second set of analyses (Run 2 in Table 4) which gives a robust indication of a sound analysis. Although the sample was contaminated with epidote and magnetite, the measured age was not affected, although the Re (ppm) may not represent the Re content within the molybdenite dated.

Titanite from the Sokolov deposit is coarse grained and euhedral. It is commonly intergrown with coarse grained euhedral magnetite, fine grained epidote and pyroxene and is thought to have formed during the main skarn phase (Fig. 10f). Back-scattered electron images show titanite varying from sub-hedral, but uncorroded and unzoned grains (Fig, 16a) through patchily zoned grains indicative of alteration (Fig. 16b) to corroded, microporous grains (Fig, 16c). There thus may be the potential for disturbance of titanite U-Pb isopte systematics. Data from U-Pb analyses (Table 5) are plotted as conventional Concordia plots, and as cumulative probability plots based on ages derived from the more accurately determined $^{206}Pb/^{238}U$ ratio (Fig. 16). In both the samples analysed the data are to some extent discordant (Fig. 16d, f) and also show evidence for spread along Concordia, such that a Concordia age could not be determined. This is consistent with resetting of the isotope systematics, probably by solution-reprecipitation processes (Putnis, 2002) as conditions were below the nominal closure temperatures for the U-Pb system in titanite (650-700°C in titanite without radiation damage; Cherniak, 1993; Frost et al., 2000). This resulted in partial loss of U and/or addition of Pb in domains within titanite crystals. In sample 68 data are close to concordant, and a lower intercept model 2 age of 326.6±4.5Ma can be defined, albeit with an anomalously high upper intercept (Fig. 16d). There is potential spread in individual analyses from around 340-310Ma (Fig. 16e). For sample SOK3 no clear intercept age could be defined (Fig. 12f). $^{206}Pb/^{238}U$ ages spread from ~330-270Ma with a slight bimodality at 295 and 310Ma (Fig. 12g).

6.5 Stable Isotope Data

The oxygen isotope compositions of epidote, garnet, hematite, magnetite, calcite and pyroxene were measured, alongside the carbon isotope composition of calcite, and sulphur isotopes in sulphides and sulphates (Table 6). From paragenetic studies it can be ascertained that garnet, pyroxene, epidote and magnetite are components of the main skarn phase of alteration. Hematite is paragenetically later than the main skarn phase and can be found as alteration of magnetite or within calcite veins.

Silicates have a general range of $\delta^{18}O$ from between 5‰ and 9‰ and in general are slightly enriched compared to magnetite $\delta^{18}O$ (Fig. 17a). The majority of the values measured from magnetite from Kachar and Sokolov range between 2‰ to 4‰. Magnetite from Sarbai ranges between 5‰ to 8‰ but only 3 analyses are available from this deposit (Fig. 17b). Hematite is depleted in ^{18}O compared to all other oxides and silicates, but again, only a relatively limited number of analyses have been conducted.

The carbon and O isotope data from calcite show two main clusters. A group of mainly Kachar calcite samples are slightly depleted in $\delta^{18}O$ (18.2‰ to 23.4‰) and strongly depleted in $\delta^{13}C$ (-12.7‰ to -7.0‰) relative to unaltered limestone (Table 6). Other calcites from all three deposits have a $\delta^{18}O$ isotope composition from 13.7‰ to 20.6‰ together with a $\delta^{13}C$ isotope composition (-4.4‰ to 2.9‰), giving compositions that lie intermediate between those of marine carbonates (Veizer and Hoefs, 1976) and that of magmatic fluids (Bowman, 1998).

The majority of the sulphides from all of the deposits have a $\delta^{34}S$ composition of near zero with a mean of 0.1±2.4‰ (1σ; excluding one outlying value of 6.6‰) and a range of between -3.8 and 6.6‰ (Fig. 17c; Table 6). For pyrite, the values for each deposit are broadly

comparable (Fig. 17d). The outlying $\delta^{34}S$ value of 6.6‰ is from paragenetically late pyrrhotite which may have included some contamination by gypsum in the mineral separate. Gypsum in cross cutting veins from the Sarbai deposits has values ranging from 4.9 to 9.6‰ (Fig. 17c).

6.6 Fluid inclusion microthermometry.

Fluid inclusions were sparse throughout the deposits, and hence only limited data of a preliminary nature can be presented here. Measurable fluid inclusions were found in pyroxene, garnet and calcite from Kachar and Sokholov. Inclusions in pyroxene where typically isolated in grain centres, consistent with a primary origin (Fig. 18a), and clearly distinguished from secondary inclusions in the same phase (Fig. 18b). They have an assemblage of aqueous liquid+vapour+halite (Lw+Sh+V) at room temperature (Fig. 18c). Inclusions in garnet occupied grain cores (Fig. 18d) or in some instances occur along oscillatory zones (Fig. 18e), again with Lw+Sh+V at room temperature (Fig. 18f,g). In calcite they occurred in relative dense groups with evidence for both primary and secondary trapping (Fig. 18h). The data show three main groups of inclusions (Fig. 19a; Table 7). A high temperature >600ºC ultrasaline fluid (between 49 and 51 wt. % NaCl eq.) occurs in pyroxene. The main skarn phase fluid with temperatures >280ºC and salinities between 10.5 - 37 wt. % NaCl equiv. occurs in pyroxene and garnet, and a late low temperature phase with temperatures > 117ºC and salinities between 20 and 23 wt. % NaCl eq. occurs in calcite.

6. Discussion

7.1 Timing of mineralisation.

SHRIMP dating of zircon from a granite-porphyry dyke (Hawkins, 2012) which clearly cross-cuts mineralisation at the Sarbai deposit yielded an age of 322.2 ± 4 Ma. The altered

rock that hosts the mineralisation at both the Sarbai and Sokolov deposits corresponds to the Sokolov and Sarbai suites of the Valerianovka Supergroup (Porotov et al., 1987). These have been interpreted as being middle Visean to late Visean in age (345.3 to 326.4 Ma) on the basis of fossil evidence by Porotov et al. (1987). These ages give an upper and lower age boundary for the mineralisation at the Sarbai deposit of between 345 Ma and 322 Ma. These relationships are seen at both the Sokolov and Kachar deposits and it is most likely that the period of mineralisation is the same. Molybdenite crosscuts the minerals of the main skarn phase and is therefore paragenetically later and thus its age of formation gives a minimum age for the mineralisation. The age of molybdenite from the Sarbai deposit was determined by Re-Os geochronology as 336 ± 1.3 Ma. This is also older, but within error of the measured age for the dacite extrusive series that hosts the mineralisation at Kachar (323 ±15 Ma K-Ar isochron; Porotov et al., 1987; 315 ± 24 Ma Rb-Sr isochron; Ronkin et al., 1993). There is potential for resetting of both K-Ar and Rb-Sr systematics by thermal events linked to the post-ore intrusive rocks.

U/Pb laser ablation dating of titanite from the Sokolov deposit gives variable ages of between 330 and 270 Ma. The oldest possible ages, and the lower intercept age for sample 68 are within error of the Re-Os age from molybdenite. The younger ages correspond to the ages calculated for the Pridorogny and Dzhabyk Karagandski intrusive series (between 290 and 285 Ma) and to the K-Ar ages calculated for the Sarbai-Sokolov series (Dymkin, 1966). These ages are younger than the Milutin series dykes that clearly cross cut mineralisation and which have a SHRIMP age of 322.2 ± 4 Ma. The titanite age records the post-ore alteration at the Sokolov deposit by the Pridorogny intrusive series which characteristically cross-cut the magnetite deposits from at 290 ± 6.2 Ma. Magmatic bodies with these ages have been interpreted as having been intruded during the post-collisional event that affected much of the Urals (Bea et al., 2002). Titanite is intergrown with the epidote and magnetite of the main

skarn phase and therefore ages determined during this study are interpreted as the result of resetting of titanite during this event. This is also consistent with the 298 ± 31 Ma Sm-Nd magnetite and apatite ages calculated for the adjacent Kachar deposit (Ronkin et al., 1993; 1997). Apatite has low closure temperatures and typically records late stage overprinting thermal events.

The relationship of the magnetite mineralisation to the diorites of the Sarbai-Sokolov series has been discussed above. Potassium-Ar dates for this series ranging from 315-286 were measured by Dymkin (1966). These Sarbai-Sokolov intrusive rocks cross cut the Sokolov and Sarbai suites of the Valerianovka Supergroup and are cross cut by the Milutin series dykes that have SHRIMP age of 322±4 Ma. This gives a range of formation of between 345 and 322 Ma. Again, K-Ar ages probably reflect Ar-loss during the thermal events resulting from the intrusion of the Milutin and Pridorogny series granitoids.

7.2 Paragenesis, alteration conditions and fluid evolution.

Pre-ore alteration assemblages preserved in limestone distal from the main ore zones include wollastonite, dioside and tremolite. Detailed assessment of the T conditions of these mineral reactions is impossible as they are continuous reactions, strongly influenced by the composition of the metamorphic fluid. However, limits can be placed because in the presence of a saline, skarn forming fluid (salinities in this case are as high as 50 wt. % NaCl eq.) water and carbon dioxide are not perfectly miscible. Figure 20a shows the phase diagram for the system H_2O-NaCl-CO_2 at 0.1GPa and 20 wt. % NaCl from Bowers and Helgeson (1983). In this system, below approximately 600°C, the water-rich fluid is limited to a maximum of ~0.1 X(CO_2) (Fig. 20b). This can be compared directly with the T-XCO_2 section of Winter (2001), which is for a pure H_2O-CO_2 fluid, as at relatively low pressures (<2kbar) the activity co-efficients of water in NaCl-H_2O-CO_2 fluids are close to unity (Schmulovich and Graham,

1996). This indicates initial diopside, and potentially wollastonite formation at ~650°C. Wollastonite may have formed at higher T and XCO2 prior to the infiltration of saline fluids into the system. Wollastonite breaks down to calcite plus quartz at~500°C, and tremolite formation at ~390-420°C. Fluid inclusion homogenisation temperatures in diopside indicate formation at temperatures slightly in excess of 600°C in the presence of saline aqueous fluid, which is consistent with the upper stability limits shown in Figure 20b.

The shift from the pre-ore assemblages to the main skarn assemblages containing magnetite and andradite garnet was driven by the ingress of iron-rich fluids as the skarn system developed. Figure 20c shows a T-log fO_2 section for the system Ca-Fe-Si-O-H-C calculated using SUPCRT92 (Johnson et al., 1992), and equations given by Zhang and Saxena (1991). In addition curves have been added for the reaction of hedenbergite and anorthite to epidote plus quartz to show the influence of Al in the system, and the reactions hedenbergite plus quartz plus magnetite, or andradite plus quartz plus magnetite to actinolite. For comparison the curve for fO_2 buffered by CO_2-graphite is shown to indicate a lower boundary for the system (graphite is absent in these skarns). The curve for fO_2 buffered by the assemblage K-feldspar-annite-magnetite is shown to indicate the constraints imposed by introducing a fluid initially equilibrated with a granitoid mineral assemblage (potentially derived from the Sarbai-Sokolov intrusive suite). Mole fraction CO_2 was set at a low value of 0.06 to reflect the constraints imposed by fluid salinity and aqueous-carbonic fluid immiscibility discussed above, although this may have varied with T and salinity during the evolution of the system. Under these conditions the lower limit of the assemblage andradite, magnetite and quartz is around~450°C and log fO_2 ~-26 where hedenbergite would form instead. In the Turgai systems the formation of andradite is almost certainly a function of the addition of Fe from the hydrothermal fluid, and hedenbergite forms only a minor component in dioside (10-20 mole %). The assemblage andradite-magnetite-quartz is then stable to

~250°C, where andradite breaks down to calcite-magnetite-quartz. Andradite could break down to form actinolite at around 450°C in the presence of free quartz. This reaction is observed at many points, but it would be limited in the absence of free quartz (rare outside of the altered volcanic rocks) by the $aSiO_2$ in the fluid, which would shift the actinolite forming reaction to lower fO_2. Later, hematite-bearing assemblages indicate the ingress of meteoric fluid, marked by the dilution seen in fluid inclusions, into the system, which would move it away from an fO_2 buffered by the main stage skarn assemblage The large excess of magnetite would either buffer the fO_2 at the hematite-magnetite boundary, or, in areas isolated from magnetite, or where all magnetite has been reacted away, allow the fO_2 to evolve to values above the hematite-magnetite boundary at a given temperature. These conditions are entirely consistent with temperatures inferred for chlorite formation at the same paragenetic stage above.

The paragenetic associations of sulphide mineralisation are also consistent with the above models. Late ore-stage calcite associated with sulphides host fluids inclusions with trapping temperatures of 250-350ºC at 500bars. The formation of pyrite in the presence of excess magnetite would buffer the fO_2, and where pyrrhotite is also present the pyrite-pyrrhotite-magnetite triple point would fix the fO_2 at ~-39 at 250°C (Ohmoto, 1972; Bowman, 1998). This is consistent with the constraints for a fluid within the andradite stability field, with fO_2 buffered buffered by an excess of fluid that equilibrated with an igneous assemblage at higher temperatures Pyrrhotite bearing assemblages give a strong constraint where they are present, but elsewhere the pyritisation of magnetite could indicate higher fO_2.

The subsequent deposition of minor amounts of gypsum alongside calcite-hematite veining indicates late-stage, more oxidised fluids interacting with the skarn system. The presence of barite, gypsum and hematite alongside supergene sulphide phases (cuprite,

greenockite) in the late phases of alteration may also be due to local ingress of large volumes of meteoric fluid into the system at temperatures below 150°C (McConnell et al., 1987).

The above discussion focuses on the main skarn calc-silicate, sulphide and oxide phases. The system used to investigate these assemblages does not include scapolite. Textural evidence suggested that scapolite alteration accompanied the late skarn and post-ore phases of alteration. The scapolite itself is marialite dominated. At these stages fluid salinities determined from fluid inclusions were in the range 35-20 and then 23-20 wt. % NaCl eq. respectively. The presence of marialitic scapolite, particular in the altered volcanic sequence is consistent with a NaCl-dominated brine being responsible for the alteration (Pan, 1998).

The constraints from phase equilibria are entirely consistent with fluid inclusion and stable isotope data. Stable isotope geothermometry using the silicate mineral assemblage was limited. Andradite and pyroxene co-exist, and should have a near identical $\delta^{18}O$ (within analytical errors – Zheng, 1993a) if deposited at the same time. A single sample from Sokolov indicated diopside-andradite equilibration at ~323-159°C (Fig. 21a). However, andradite typically post-dates diopside and so equilibrium could not be texturally established for these phases. Magnetite-calcite mineral pairs provided more precise T constraints using the fractionation factors of Zheng et al. (1991) and Zheng (1993b). This indicates calcite and magnetite precipitation from ~520±25°C to 170±7°C (Fig. 21a). Although these temperatures could not be assessed for equilibrium on the basis of textural evidence, they are at least consistent with phase equilibria. Geothermometry using sulphide mineral pairs is also hampered by the lack of good textural evidence for equilibrium and only minor differences in fractionation factors (Ohmoto et al., 1979). A single sample (VAR-SA-02) gave a temperature consistent with equilibrium between pyrite and pyrrhotite at ~250°C, but others were inconsistent with equilibrium being established.

Figure 19b shows the possible pressure temperature path of the skarn forming fluid based on fluid inclusion evidence from ultra-saline fluids at near 600°C to high salinity, main skarn phase fluids between 48-20 wt. % NaCl equiv. The high temperatures and salinities of the early skarn phase are beyond the experimentally calibrated range of currently available equations of state and empirical equations for isochore location. True estimates of the total dissolved solids in solution are likely to be higher than salinities estimated assuming a pure NaCl solution (Sterner et al., 1987; Oakes et al., 1990). Sodic alteration and chlorine-rich mineral phases (apatite, pyrosmalite-(Fe), scapolite; Fig. 8) that are found within the Sokolov, Sarbai and Kachar deposits indicate that fluid that formed them was enriched in Na, Cl and Si. Fluid inclusions in diopside from Kachar homogenise at ~600°C, from a hypersaline (~50 wt. % NaCl) brine with minimal CO_2 content. This value is close to the maximal stability of diopside at 1 kbar in the presence of water-rich fluids (Fig. 20B; Winter, 2001), and suggests minimal pressure correction is necessary to T_h to gain a trapping T. This would suggest early skarn formation at ~700bars, consistent with a subvolcanic environment. Subsequent cooling of the system to around 200°C, was accompanied by dilution of the fluids to ~20 wt. % NaCl eq. The main‘ skarn fluid had between 30 and 40% wt.% NaCl eq. and late calcite veins contained between 20 and 23% wt. % NaCl eq. (Fig.19).

7.3 Fluid sources.

Figure21b shows the oxygen and carbon isotopic composition of skarn and vein calcites. A group of metamorphosed limestones from Kachar, along with a limited number of samples from Sarbai define a group at high $\delta^{18}O$ (13.7 to 15.9‰) and low $\delta^{13}C$ (-7.0 to -10.8‰). These represent a depletion in $\delta^{13}C$ of between 7 and 14 ‰ and a relatively minor depletion of $\delta^{18}O$ compared to marine limestone. Equilibrium decarbonation reactions can produce significant $\delta^{13}C$ depletion but only a limited $\delta^{18}O$ depletion (Valley 1986). The values

measured from the Kachar deposit are characteristic of calcite produced by equilibrium decarbonation by silicate forming reactions, illustrated in Figure 21b using the equations of Bowman (1998), and consistent with the addition of silica to the limestone from metasomatic fluids and the formation of wollastonite (Fig. 10a).

The second grouping of calcite carbon and oxygen stable isotope composition are intermediate between the field for magmatic calcite (i.e. calcite precipitated from magmatic fluids) and that for marine limestones. Figure 21b shows a range of curves representing the composition of calcite precipitated from fluids that represent mixtures between a magmatic fluid, and one that had derived its carbon and oxygen isotope signature from marine limestone, calculated from the equations of Bowman (1998) assuming a temperature of 350°C and using the fraction factors of Zheng (1993b). The data are consistent with calcite precipitation from fluids with a mixture of igneous-equilibrated and limestone C and O isotopes. The implication of relatively high $X(CO_2)$ in the metasomatic fluid that has not been observed in fluid inclusions may indicate a stage of fluid circulation not sampled by inclusions. However, the mixing calculations are of necessity simplified, and some of the departures from the fluid composition suggested from fluid inclusion studies and consideration of the position of the water-CO_2 solvus inferred here, may be accounted for by advective transport and isotopic exchange models (Bowman, 1998). Equally, it has been shown that both mixing trends and apparent advective isotopic exchange fronts can be produced by the healing of fractures in marble calcite by calcite precipitated from externally derived fluids (i.e. mechanical mixing without isotopic exchange; Lewis et al., 1998), which would account for the mixing trend between marine limestone and calcite deposited from fluids with magmatic equilibrated C and O isotope compositions without the need for high $X(CO_2)$ fluids. An additional possibility would be the mixing of oxygen derived from decarbonated limestone with an ^{18}O depleted fluid of non-magmatic origin. Given the high

salinities preclude unmodified meteoric waters, the most likely candidates are waters with salinity derived from dissolution of evaporites. Fluids that had interacted with typical marine evaporites (with a high gypsum/anhydrite content) would be expected to have relatively high $\delta^{18}O$ reflecting the composition of marine sulphate. They are not therefore, likely candidates.

Oxygen isotope data from oxide and silicate phases are also consistent with deposition from, or interaction with, an^{18}O depleted fluid that had interacted with marine limestone at a range of temperatures and water-rock ratios. Figure 21c shows the calculated oxygen isotope composition of fluids in equilibrium with the various minerals at temperatures derived from co-genetic magnetite-calcite pairs, fluid inclusion data or phase equilibria. Calculated fluid $\delta^{18}O$ compositions for equilibrium with magnetite lie dominantly in the range 6 to 12‰, overlapping and on the edge of the magmatic fluid range. Some of the heavier fluid compositions may represent mixing of ^{18}O depleted oxygen with oxygen derived from dissolution and decarbonation of the host limestones. All other calculated fluids are consistent with an ^{18}O depleted fluid at temperatures between 200 and 600 °C. The composition of fluid equilibrated with magnetite is not sensitive to T down to around 100°C (±1‰), but it is significantly more so for the main skarn silicate phases analyses (pyroxene, epidote, andradite). These phases, however, clearly did not form at such low temperatures. Again, the most likely candidates for the ^{18}O depleted fluid are igneous equilibrated (and potentially magmatic) waters, or formation waters.

The sulphur isotope composition of minerals precipitated from hydrothermal solutions is dependent on the speciation of sulphur within the hydrothermal fluid, and hence on the T, P, pH and fO_2 conditions of mineralisation (Ohmoto et al., 1972). For the main sulphide stage paragenesis of pyrite+pyrrhotite deposition in the presence of an excess of magnetite the fluid composition would be buffered close to pH 6 and log fO_2 -38. Under these conditions there would be minimal fractionation in $\delta^{34}S$ between pyrite and pyrrhotite and the H_2S in the fluid

from which they formed (within 1.8‰). This suggests that the sulphur in the metasomatic fluid at this stage was derived from magmatic sources (Figure 21d). Assuming precipitation from a H_2S-rich fluid (i.e. with low pH and low fO_2) with an isotopic value of 0 ‰ $\delta^{34}S$ (magmatic) the small variations of pyrite and pyrrhotite can be largely explained by changing temperatures. More depleted and enriched $\delta^{34}S$ values, however, require a different explanation. Assuming a near magmatic total sulphur isotope value of the fluid ($\Sigma\delta^{34}S \approx 0‰$) the enriched values measured from pyrrhotite and chalcopyrite may have been produced at low oxygen fugacities where an increase in pH produced an increase in $\delta^{34}S$ composition of sulphides. Pyrrhotite is not ubiquitous in sulphide assemblages in the Turgai skarns, and assemblages of pyrite plus magnetite may indicate conditions under which the mineralising fluid had significant sulphate contents, leading to large negative fractionation factors. This could suggest a fluid with a positive $\delta^{34}S$ (upto +20‰), which could indicate evaporitic sources of sulphur. However, sulphate mineral assemblages (barite, gypsum) only occur at very late stages (probably linked to the oxidation of pyrite during weathering), fractionation factors below barite saturation are small (Ohmoto, et al., 1972; Rye and Ohmoto, 1974), and pyrrhotite does occur in a number of places, alongside magnetite and pyrite (Fig. 12). We therefore infer a magmatic sulphur source dominated in Turgai skarns, although ^{34}S enriched sulphur sources cannot be entirely ruled out. Heavy $\delta^{34}S$ values in sulphides which occur in a number of IOCG systems and provide strong evidence for the inclusion of evaporitic sulphur (Barton, 2014) have not been observed here. The enriched $\delta^{34}S$ values of gypsum (up to $\delta^{34}S$=12‰) also found within late cross cutting veins are consistent with precipitation from a fluid with a $\Sigma\delta^{34}S$‰ of near zero at high fO_2 (Ohmoto et al., 1972; Rye and Ohmoto, 1974). Late stage hematisation of the ore at the same time as the formation of gypsum veins indicates that the skarn forming system moved to more open system, externally buffered fO_2 conditions, possibly as a result of the dissipation of initial fluid over pressures and the

subsequent ingress of meteoric fluids from low hydrothermal (<150°C) to weathering conditions. Under conditions of pyrite saturation the shift in fluid chemistry towards sulphate mineral saturation would lead to the precipitation of sulphates enriched in ^{34}S relative to the fluid of between ~7 to 26‰. The deposition of gypsum with $\delta^{34}S$ between 5 and 13‰ under these conditions is still entirely consistent with a magmatic source for sulphur, probably indirectly via oxidation of the sulphide mineral assemblage.

7.5 Implications and global comparisons.

The Turgai deposits are skarns with ore dominantly developed as limestone replacement with smaller volumes of direct replacement of metavolcanic rocks. We would argue that the evidence presented here strongly supports a magmatic origin for the initial alteration fluids, although the involvement of external fluids which have interacted with evaporites cannot be ruled out, and may be necessary to produce the sodic alteration assemblages. The presence of marialitic scapolite and an extensive halo of albite alteration are common in skarn systems. Pan (1998) summarised the occurrence of scapolite in skarns globally and concluded that the occurrence of extensive marialitic-scapolite, albite, K-feldspar and chlorite in skarn, alongside large volumes of metasomatic iron oxides with super-imposed sulphides, is suggestive of links to the Iron oxide-copper-gold class (Hitzman et al., 1992; Williams et al., 2005; Herrington et al., 2002). The Turgai deposits were included in this class by Barton and Johnson (1996) and Williams et al., (2005), although by the criteria of Williams et al. (2005), the deposits are not IOCG mineralisation since they lack economic concentrations of copper. Barton (2014) pointed out that this later criteria is societal rather than geological, and that Cu-Au barren to mineralisaed systems form a continuum. Corriveau (2007) would regard them as representing IOCG-style mineralisation

of the 'iron-skarn sub-type'. Skarn-type alteration has been described from IOCG systems (e.g. Wang and Williams, 2001), and it is notable that a number of iron oxide-apatite deposits (IOA) including both Kirunavaara (Sweden) and El Laco (Chile) have either diopside associated with magnetite (El Laco; Nystrom and Henriquez, 1994; Sillitoe and Burrows, 2002), or have been inferred to have had primary diopside now replaced by actinolite (Kirunavaara; Blake, 1992). The skarn mineralisation in the Turgai area may therefore have links to at least the IOA deposits and the early magnetite mineralisation seen in IOCG deposits, with the defining difference being the replacement of, or development of veins, stockworks and breccias in, silicate volcanic rocks in the IOA and IOCG systems, rather than limestone (e.g. Smith et al., 2007). Phosphorus contents in the bulk ore are also comparable between Turgai skarns and Kirunavaara iron ore (≤1% P at Kirunavaara; Carlon, 2000; 0.07-0.3% P in the Turgai skarns; Sokolov and Grigor'ev, 1977). There can be no doubt, however, that the Turgai magnetite deposits are formed by metasomatic replacement. This highlights an issue in the debate over the possible magmatic origin of the IOA deposits. A 'magmatic' origin, via liquid immiscibility, for Kirunavaara and related deposits has been proposed by workers such as Geijer (1931), Nyström, (1985), Nyström & Henriquez, (1994) and Naslund et al. (2002). Subsequent workers have disputed this with models beginning with exhalative deposition (Parak, 1975), and more recently developed to metasomatic replacement (Blake, 1992; Bookstrom, 1995; Sillitoe, 2003; Williams et al., 2005). The most recent argument for a magmatic origin for the Kiruna-type ores of Grangesburg, Sweden, was presented by Jonsson et al. (2013) on the basis of magnetite $\delta^{18}O$ values ranging from -0.4 and +3.7‰. This range overlaps, however, with range of -1.45 to +7.37‰ for skarn magnetite presented here, and cannot be used a definitive evidence for magmatic origin. A number of arguments for magmatic origin at El Laco, Chile, have stated that hydrothermal alteration must destroy primary textures, and the preservation of igneous and volcanic textures in the magnetite there

must indicate primary magmatic crystallisation (Naslund et al., 2002). The preservation of features by perfect volume-for volume replacement of protoliths in the Turgai skarns definitively refutes this hypothesis. The magnetite ores of the Urals were clearly formed by hydrothermal systems involving high salinity brines, and a similar origin is likely for many IOA deposits. In all areas, however, there remain discussions about the potential for single pass magmatic-hydrothermal systems to supply the necessary flux of Na, Cl and Fe, which have lead to concepts relating mineralisation to alternative fluid sources (Barton and Johnson, 2000). Barton et al. (1996, 2000, 2014) suggested that fluids which derived their salinity and other fluid components from sedimentary evaporites may play an important role in the transport of iron and other transition metals. The reported proximity of the Turgai deposits to large evaporite units (Porotov et al., 1987) lead to the suggestion that these were the source of the large quantities of NaCl required to transport iron in solution. Evaporites containing enough NaCl to provide the necessary amount of Cl^- to transport iron would also contain appreciable amounts of $\delta^{34}S$ enriched sulphur derived from seawater, primarily contained in gypsum and anhydrite. For the time periods considered (350 and 315 Ma) seawater sulphates had a $\delta^{34}S$ signature of between 18.1 and 14.8 ‰ (Kampschulte and Strauss, 2004). The Turgai suphides have a consistent near zero ‰ $\delta^{34}S$, and the $\delta^{34}S$ of gypsum is also consistent with it having precipitated from a fluid with a total $\delta^{34}S$ of near zero. This strongly supports a magmatic source for sulphur, although heavier sulphur input cannot be entirely ruled out. The involvement of external brines may be indicated by the extensive sodic alteration halo surrounding the deposits. Initial alteration of the host volcanic sequence included K-feldspar, which textural evidence indicates preceded albite and scapolite (Fig. 13e). This is consistent with the expected alkali composition of high temperature igneous equilibrated brines. For sodic alteration brines must depart from Na/K ratios determined by equilibration with two feldspars (Oliver et al., 2004). This can be achieved via mixing with NaCl-rich brines, by

aqueous-carbonic fluid immiscibility, or by assimilation of evaporites into the magma prior to fluid exsolution (Oliver et al., 2004). All of these are possible in the Turgai skarns.

Significant potential sources of magmatic fluid do occur in the Turgai area. Bekmuhametov et al. (2004) have modelled a large gabbroic intrusion underneath the Valerianovka zone as a common source for all of the smaller bodies of the Sarbai-Sokolov intrusive series. The Sarbai-Sokolov series includes gabbroic to granodioritic intrusions, all of which contain apparently primary biotite (Ksenofontov and Ivlev, 1971) indicating significant water contents. Evolution by fractional crystallisation would have provided mechanism to drive the exsolution of large volumes of magmatic brine, and typical porphyry style deposits do occur in the area (Benkala). An association with the Sarbai-Sokolov series is also supported by the temporal relationship of ore formation (inferred to be around 336 ± 1.3 Ma) with the crystallisation age of intrusions (345 Ma to 322Ma – Hawkins, 2010). Detailed calculation of the volume of NaCl alteration is limited by the lack of exposure. However, assuming an Fe content of saline brines of 100,000ppm (10 wt. %) in a fluid of 50 wt. % NaCl equivalent (consistent with fluid inclusion analyses from Yardley (2005) and Smith et al. (2013)), then the 3Gt of Fe_2O_3 within the Turgai skarns could be formed from a magmatic fluid phase derived from approximately 233km^3 of basic to intermediate magma (i.e. a cube ~6.2km along each side). This assumes a magma water content of 4 wt. % (in order to stabilise biotite in basic to intermediate magma – Webster et al., 1999; Beard et al., 2004) declining to 1 wt. % in the final rock. This would require that only 5% of the total Fe content of the magma in the same volume was abstracted to the fluid phase, assuming an Fe content of 8.6% in the basic to intermediate rocks of the Sarbai-Sokolhov intrusive series (based on analyses from Hawkins, 2012). More efficient chloride removal from the magma would be necessary (~75% of available chloride extracted to the hydothermal fluid), but this is consistent with magma-fluid partitioning of halogens (Webster et al., 1999). Reducing the

fluid salinity to 30 wt. % NaCl eq., and the Fe content of the hydrothermal fluid to 1 wt .% would double the necessary volume of source rock. Efficient focussing of fluid from such volumes into the skarn zone can achieved as a result of the pressure drop within the skarn relative to surroundings because of reaction-driven porosity generation (Balashov and Yardley, 1998). These simple mass balance calculations are minima for the true fluid flux required for ore deposition, as they assume 100% efficient deposition of Fe from the hydrothermal fluid. They do, however, indicate that the required fluid flux would be possible from an evolving magmatic source.

Global examination of the distribution of IOA and IOCG systems through geological time has lead to suggestions that IOA deposits formed during subduction and continental convergence and the intrusion of related granitoids, whilst IOCG systems formed in post-collisonal, anorogenic settings related to sub-continental lithospheric mantle sourced magmatism arising from either mantle underplating or plume activity (Groves et al., 2010). Richards and Mumin (2013) summarised the principal tectonic environments of formation as ranging from back-arc through intra-arc to post-collisional extension and suggested the temporal distribution of deposits may relate to secular changes in the seawater sulphate concentration, and hence sulphur cycling through subduction systems. In the Turagi area the data from molybdenite Re-Os systematics suggests sulphide mineralisation took place at 336 ± 1.3Ma. Iron oxide mineralisation must have predated this, with the U-Pb systematic of titanite being reset by post-depositional events from 326.6± 4.5Ma. The date of sulphide mineralisation, which may not have significantly post-dated magnetite, as there is no evidence for older ages preserved in titanite, is synchronous with the emplacement of the Sarbai-Sokolov suite, and younger than the Kiutin series. The Priodorogny and Dzhabyk-Karagandski intrusive series may be responsible for the late thermal overprint observed in titanite. Other major Fe deposits in the southern Urals are also of a similar age. Both the

Magnitogorsk and Mali Kuibas deposits have been suggested to have formed from 342–337Ma, contemporaneous with the age of the Magnitogorsk intrusion (Fershtater, 1997; 2007; Fig. 22). In the Magnitogorsk district, the bulk of the ores are true skarn replacement ores, although a subordinate, and characteristically Ti-rich, orthomagmatic magnetite mineralisation is recorded in deeper, gabbroic parts of the intrusions (Fershtater et al., 2005). The Valerianovskoe zone or Valerianovka arc, together with the subordinate Irgizkaya and Alexandrovskaya arcs (Fig. 1) form long, roughly north-south and NNE-SSW trending iron-rich belts which are mirrored by the iron-deposits developed in Carboniferous rocks in the sub-parallel Magnitogorsk zone. The deposits from these belts are all strikingly similar in size, shape, mineralogy and paragenesis (Herrington et al., 2002). In current tectonic models at the time of formation the eastern belts of Irgizkaya, Alexandrovskaya and Valerianovka were separated from the Magnitogorsk arc by an open Uralian ocean located where the Troitsk fault lies, and the two iron-rich terranes only came together during the collision of Laurussia with the Kazakh plate. Figure 22 shows the range of ages of mineralisation related to magmatism from previous work and as determined here where a distinct period of between 340 and 330 Ma is noted for the age of iron mineralisation. Fershtater et al. (2007) interpreted the geochemical signatures of the rocks belonging to the Magnitogorsk intrusive series as showing both subduction-and rift-related signatures. Hawkins (2012) suggested that the mafic bodies of the Sarbai-Sokolov series may have been intruded into the Valerianovka zone as a result of back-arc rifting eastwards from the Valerianovka arc. Similarly in the Magnitogorsk zone this period of magmatism is thought to be related to a supra-subduction rift and the related volcanic–plutonic magmatism (Fershtater et al. 2007). These settings would not, however, explain the similarities of styles of intrusions and mineralisation with formation ages within error. This appears to require a Urals-wide event suggesting the Uralian Ocean may have been closed by the time that these rocks and associated mineralisation were

formed. We suggest that both intrusive series and their associated skarn deposits were formed in similar tectonics settings as a result of magmatism during the final or post-collision stages of the Uralian orogeny (Hawkins, 2012).

7. Conclusions

The magnetite deposits of the Turgai zone, Kazakhstan, are unequivocally Fe skarn-type deposits, with characteristics including late stage sulphide mineralisation and an extensive sodic (albite+scapolite) alteration halo that suggest they may have genetic links to the IOCG deposit class. The characteristics of mineral assemblages and fluid inclusions, and stable isotope geothermometry using oxygen and sulphur isotopes suggest initial formation of pre-skarn alteration at >600ºC, skarn alteration and magnetite mineralisation from ~550 to 250ºC, and post-ore alteration and sulphide mineralisation from ~250 to 150ºC. The associated fluids were initially hypersaline (~45-50wt. % NaCl eq.), and became progressively more dilute, with salinities of ~20wt. % NaCl eq. in late stage calcite veins. The $\delta^{18}O$ composition of magnetite and skarn silicates, and the $\delta^{18}O$ and $\delta^{13}C$ composition of calcite are consistent with the infiltration of ^{18}O depleted fluids into limestone. The $\delta^{34}S$ compositions of sulphides and sulphates are consistent with magmatic sources of sulphur if crystallisation took place at relatively low fO_2. Some mixing with isotopically heavier evaporitic sulphur may have occurred, but this did not dominate the ore system. Sources of Na-rich brine may be necessary, however, to explain the large sodic alteration halo developed in volcanic rocks surrounding the skarns. Geochronological studies using Re-Os syematics of molybdenite and U-Pb systematics of titanite suggest formation of the skarn systems between ~337 to 322Ma, coinciding with the intrusion of the Sarbai-Sokolov magmatic series, and subsequent modification during later thermal events to ~270Ma.

The similarities between the Turgai skarns and some IOA and IOCG systems suggest genetic links with at least the magnetite-rich members of these deposit types, and support arguments for a magmatic hydrothermal origin. The similarity in time of formation between the Turgai deposits and the Magnitogorsk skarns in the western Urals suggest that a similar process was operating Urals-wide during their genesis, and indicate that their formation may have taken place after the main orogenic assembly of the Kazakh collage and East European Craton.

Acknowledgements

We would like to thank the CERCAMS project and Reimar Seltmann in particular at the Natural History Museum, London and Jim Coppard, formerly of Anglo American Plc for financially supporting this project. Sokolosko-Sarbaiskiy Gorno-Obagatitelnoe Objedineniye (The Sokolov-Sarbai Mining Production association, SSMPA) allowed access to the open pits for fieldwork and sampling. The work has benefitted from discussion and fieldwork with J. Coppard, L. Mordberg, J. Alitaalo, G. Fershtater. Stable isotope work was supported by NERC Facilities grant **IP/1048/0508**. AJB is supported by NERC Facilities funding at SUERC. Re-Os isotope analyses were carried by R. Creaser at the University of Alberta, Canada. Craig Storey assisted with processing of LA-ICPMS U-Pb analyses of titanite. We would like to thank R. Seltman and M. Barton for constructive reviews which helped improve this manuscript.

References

Bakker RJ. Package FLUIDS 1. Computer programs for analysis of fluid inclusion data and for modelling bulk fluid properties. Chem. Geol. 2003; 194: 3-23.

Balashov, VN, Yardley, BWD. 1998. Modeling metamorphic fluid flow with reaction-compaction-permeability feedbacks. American Journal of Science, 298, 441-470.

Barton MD, Johnson DA. Evaporitic-source model for igneous-related Fe oxide–(REE-Cu-Au-U) mineralization. Geology 1996; 24: 259–262.

Barton MD, Johnson DA. 2000. Alternative brine sources for Fe-oxide(-Cu-Au) systems: Implications for hydrothermal alteration and metals. In: Porter, T.M. (ed) Hydrothermal Iron Oxide Copper-Gold and Related Deposits: A Global Perspective, Adelaide, Australian Mineral Foundation, p. 43-60.

Barton MD. 2014. Iron Oxide(–Cu–Au–REE–P–Ag–U–Co) Systems. Treatise on Geochemistry, 2nd Edition, 515-541.

Bea F, Fershtater GB, Montero P. 2002. Granitoids of the Uralides Implications for the Evolution of the Orogen. In: Brown, D., Juilin, C. and Puchkov, V. (eds) Mountain Building in the Uralides: Pangea to Present, Geophysical Monograph 132 , American Geophysical Union, p. 221-232.

Beard, JS, Ragland, PC, Rusher, T. 2004. Hydration Crystallization Reactions between Anhydrous Minerals and Hydrous Melt to Yield Amphibole and Biotite in Igneous Rocks: Description and Implications. The Journal of Geology, 112, 617–621

Bekmuhametov AE. 2004. Iron ore deposits of the Turgai basin. In: Halls, C., Seltmann, R. and Dolgopolova, A. (eds) Altas of mineral deposit models of the Republic of Kazakhstan, Almaty, 142pp.

Blake K. 1992. The petrology, geochemistry and association to ore formation of the host rocks of the Kiirunavaara magnetite- deposit, northern Sweden. PhD thesis, University of Wales, Cardiff.

Bodnar RJ. Revised equation and table for determining the freezing point depression of H2O-NaCl solutions. Geochim. Cosmochim. Acta 1993; 57:683-684.

Bodnar RJ. Synthetic fluid inclusions: XII. The system H_2O-NaCl. Experimental determination of the halite liquidus and isochores for a 40 wt % NaCl solution. Geochim. Cosmochim. Acta, 1994; 58:1053-1063.

Bookstrom A. Magmatic features of iron ores of the Kiruna type in Chile and Sweden: ore textures and magnetite geochemistry: A discussion. Econ. Geol. 1995; 90:469-475.

Bowers TS, Helgeson HC. Calculation of the thermodynamic and geochemical consequences of nonideal mixing in the system H_2O-CO_2-NaCl on phase relations in geologic systems: Equation of state for H_2O-CO_2-NaCI fluids at high pressures and temperatures, Geochim. Cosmochim. Acta, 1983; 41:1247-1275.

Bowman JR. 1998. Stable-isotope systematics in skarns. In: Lentz, D.R. (ed) Mineralized intrusion-related skarn systems, Short course volume 26, mineralogical association of Canada, p.1-49.

Brown D, Juhlin C, Puchkov V (eds). 2002. Mountain Building in the Uralides. American Geophysical union, Geophysical monograph, p. 132.

Brown D, Puchkov V, Alvarez-Marron J, Bea F, Perez-Estaun A. 2006. Tectonic processes in the Southern and Middle Urals: an overview. In: Gee DG, Stephenson, RA (eds). European Lithosphere Dynamics. Geological Society, London, Memoirs, 2006; 32: 407-419.

Carlon C.J. (2000) Iron oxide systems and base metal mineralisation in northern Sweden. In *Hydrothermal iron oxide copper-gold and related deposits: a global perspective*, (ed. T.M. Porter) Aust. Min. Found., Glenside, Australia pp. 283–296.

Cathelineau M. Cation site occupancy in chlorites and illites as a function of temperature. Clay Minerals, 1988; 23:471-485.

Cherniak DJ. Lead diffusion in titanite and preliminary results on the effects of radiation-damage on Pb transport. Chem. Geol. 1993; 110:177-194.

Chou I-M. Phase relations in the system NaCl-KCl-H_2O. III: Solubilities of halite in vapor-saturated liquids above 445ºC and redetermination of phase equilibrium properties in the system NaCl-H_2O to 1000ºC and 1500 bars. Geochim. Cosmochim. Acta, 1987; 51:1965-1975.

Chuguevskaya OM. The genetic features of the Sarbai and Yrltai magnetite deposits in Turgai. Autoref. Diss. Kand. Geol. Miner. Nauk, Alma Ata 1969, (in Russian).

Corriveau L. Iron oxide copper-gold deposits: a Canadian perspective, In: Goodfellow W (ed), Mineral Deposits of Canada: a Synthesis of Major Deposit-Types, District Metallogeny, the Evolution of Geological Provinces and Exploration Methods, Geological Association of Canada, Mineral Deposits Division, 2007; Special Volume 5, p. 307-328.

De Caritat P, Hutcheon I, Walshe JL. Chlorite geothermometry: a review. Clays and Clay Minerals, 1991; 41: 219-239.

Dymkin AM. 1966. The petrology and origin of the magnetite deposits of Turgai. Nauka Press, Novisibirsk (in Russian).

Einaudi MT, Meinert, LD, Newberry RJ. Skarn Deposits. Econ. Geol. 1981; 75th Anniversary Volume: 317-391.

ENRC (2013) Eurasian Natural Resources Corporation PLC, Annual report and accounts 2012. 194pp. http://www.enrc.com/investors/financial-operational-reports.

Fershtater GB, Montero P, Borodina NS, Pushkarev EV, Smirnov VN, Bea F. Uralian magmatism: an overview. Tectonophysics, 1997; 276:87-102.

Fershtater GB, Kholodnov VV, Pribavkin SV, Borodina NS, Bocharnikova TD, Gottman IA. Riftogenic Magmatism and Iron Ore Deposition in the South Urals. Geology of Ore Deposits, 2005; 47:382-402.

Fershtater GB, Krasnobaev AA, Bea F, Montero P, Borodina NS. Geodynamic Settings and History of the Paleozoic Intrusive Magmatism of the Central and Southern Urals: Results of Zircon Dating. Geotectonics, 2007; 41:465–486.

Frost BR, Chamberlain KR, Schumacher JC, Scott DJ, Moser DE. 2000. Sphene (titanite); phase relations and role as a geochronometer. Chem. Geol. 2000; 172:131-148.

Geijer P. 1931. Berggrunden inom malmtrakten Kiruna-Gallivare- Pajala. Sveriges Geologiska Undersökning, Series C, p. 366.

Groves DI, Bierlein FP, Meinert LD, Hitzman M. 2010. Iron Oxide Copper-Gold (IOCG) Deposits through Earth History: Implications for Origin, Lithospheric Setting, and Distinction from Other Epigenetic Iron Oxide Deposits. Econ. Geol. 2010; 105:641-654.

Hawkins T, Herrington R, Smith M, Maslenikov V, Boyce A. 2010. The Iron Skarns of the Turgai Belt, Northwestern Kazakhstan. In: Porter TM, (ed.), Hydrothermal Iron Oxide Copper-Gold and Related Deposits: A Global Perspective, v. 4 - Advances in the Understanding of IOCG Deposits; PGC Publishing, Adelaide, pp. 461-474.

Hawkins T. (2012) The genesis and tectonic setting of the magnetite skarn deposits of the Turgai belt, north-western Kazakhstan. Unpublished PhD thesis, University of Brighton. 362pp.

Herrington R, Smith M, Maslennikov V, Belogub E, Armstrong R. 2002. A short review of Palaeozoic hydrothermal magnetite Iron-oxide deposits of the south and central Urals and their geological setting. In: Porter TM (ed.) Hydrothermal Iron Oxide Copper-Gold and related deposits: A Global Perspective, PGC Publishing, 2, 343-353.

Herrington R, Zaykov VV, Maslennikov VV, Brown D, Puchkov VN. Mineral Deposits of the Urals and Links to Geodynamic Evolution. Econ. Geol. 2005a; 100th Anniversary Volume: 1069-1095.

Herrington RJ, Puchkov VN, Yakubchuk AS. A reassessment of the tectonic zonation of the Uralides: Implications for metallogeny. Geol. Soc. London Spec. Publ. 2005b; 248: 153-166.

Hitzman M, Oreskes N, Einaudi MT. Geological characteristics and tectonic setting of Proterozoic iron oxide (Cu-U-Au-REE) deposits. Precamb. Res. 1992; 58:241-287.

Johnson JW, Oelkers EH, Helgeson HC. SUPCRT92: a software package for calculating the standard molal thermodynamic properties of minerals, gases, aqueous species and reactions from 1 to 5000 bars and 0 to 1000°C. Comp. and Geosci. 1992; 18:899-947.

Jonsson E, Troll V, Hogdahl K, Harris C, Weis F, Nilsson K, Skelton A. Magmatic origin of giant 'Kiruna-type' apatite-iron-oxide ores in Central Sweden. Scientific Reports, 2013; 3:1644, 1-8.

Kampschulte A, Strauss H. The sulfur isotopic evolution of Phanerozoic seawater based on the analysis of structurally substituted sulfate in carbonates. Chem. Geol. 2004; 204:255–286.

Ksenofontov OK, Ivlev AI. 1971. The magmatism and metamorphism of the Turgai trough, In: The Geology of the USSR, Vol 34 Book 2, Nedra Press, Moscow, p.9-141 (In Russian).

Leake BE, 21 members of the IMA CNMMN Subcommittee: Nomenclature of Amphiboles. Report of the Subcommittee on Amphiboles of the International Mineralogical Association Commission on New Minerals and Mineral Names. Mineral. Mag. 1997; 61:295–321.

Lewis S, Holness M, Graham C. Ion microprobe study of marble from Naxos, Greece: Grain-scale fluid pathways and stable isotope equilibration during metamorphism. Geology, 1998; 26:935-938.

Lowell GR, Noll jr., PD. Fe-Cu-Au-bearing scapolite skarn in moat sediments of the Taum Sauk Caldera, southeastern Missouri, USA, Mineral. Mag. 2001: 65:373–396.

Ludwig KR. 2003. Isoplot 3.00. Berkeley Geochronology Center, Special Publication, 4 , 70.

Mathur R, Marschik R, Ruiz J, Munizaga F, Leveille RA, Martin W. Age of mineralization of the Candelaria Fe oxide Cu-Au deposit and the origin of the Chilean iron belt, based on Re-Os isotopes. Economic Geology: 2002: 57:59-71.

McConnell JDC, Astill DM and Hall PL. The pressure dependence of the dehydration of gypsum to bassanite. Mineral. Mag. 1987: 51: 453-457.

McCrea JM. On the isotopic chemistry of carbonates and a paleotemperature scale. J. Chem. Phys. 1950; 18:849–857.

Meinert LD.1992. Skarns and skarn deposits. Geoscience Canada, 19, 145-162.

Naslund HR, Henriquez F, Nyström JO, Vivallo W, Dobbs FM. 2002. Magmatic iron ores and associated mineralisation: examples from the Chilean high Andes and coastal Cordillera. In: Porter TM (ed.) Hydrothermal Iron Oxide Copper-Gold and Related Deposits; A Global Perspective, 2. Adelaide: PGC Publishing, pp. 207-226.

Nyström JO. Apatite iron ores of the Kiruna field, northern Sweden: magmatic textures and carbonatitic affinity. GFF. 1985; 107:133-141.

Nyström JO, Henriquez F. Magmatic features of iron of the Kiruna type in Chile and Sweden: ore textures and magnetite geochemistry. Econ. Geol. 1994; 89:820-839.

Oakes C.S., Bodnar R.J. and Simonson J.M. (1990) The system NaCl-$CaCl_2$-H_2O .1. The ice liquidus at 1 atm total pressure. *Geochim. Cosmochim. Acta*, **54**, 603-610.

Ohmoto H. Systematics of sulphur and Carbon isotopes in Hydrothermal Ore Deposits. Econ. Geol. 1972; 67:551-578.

Ohmoto H, Rye RO. 1979. Isotope of sulfur and carbon, In: Barnes, H. L. (ed) Geochemistry of Hydrothermal deposits, John Wiley & Sons, 509-567.

Pan Y. 1998. Scapolite in Skarn deposits: petrogenetic and geochemical significance. In: Lentz DR (ed.) Mineralized intrusion-related skarn systems, Short course volume 26, mineralogical association of Canada, 169-209.

Parak T. Kiruna iron ores are not 'intrusive magmatic ores of the Kiruna type'. Econ. Geol. 1975; 70:1242-1258.

Pollard P. Sodic(–calcic) alteration in Fe-oxide–Cu–Au districts: an origin via unmixing of magmatic H_2O–CO_2–NaCl ± $CaCl_2$–KCl fluids. Mineral. Dep. 2001; 36: 93-100.

Poltavets YA. 1987. The Barjaghsu deposit In: Ovchinnikov LN and Dymkin AM (eds.) Ore formations of the Urals, The Turgai depression, Sverdlovsk. (In Russian).

Porotov GS. 1987. Geology of the Kachar-Davidov belt. In: Ovchinnikov LN, Dymkin AM (eds.) Ore formations of the Urals, The Turgai depression, Sverdlovsk, 160-167. (In Russian)

Porotov GS, Dymkin AM, Poltavets YA. 1987. The Kachar deposit. In: Ovchinnikov LN, Dymkin AM (eds.) Ore formations of the Urals, The Turgai depression, Sverdlovsk, 167-190. (In Russian).

Pumpyanskiy AM, Viryuchev SI, Samarkin GN. The Glubochensk magnetite deposits, Int. Geol. Rev. 1985; 93-101.

Putnis A. Mineral replacement reactions: from macroscopic observations to microscopic mechanisms. Mineral. Mag. 2002; 66; 689-708.

Richards JP, Mumin AH. Magmatic-hydrothermal processes with an evolving Earth: Iron oxide-copper-gold and porphyry Cu±Mo±Au deposits. Geology, 2013; 41:767-770.

Robinson BW, Kusakabe M. Quantitative preparation of SO2 for $^{34}S/^{32}S$ analysis from sulfides by combustion with cuprous oxide: Analytical Chem. 1975; 47: 1179-1181.

Ronkin YL. 1989. Sr isotopes as indicator of the magmatic evolution of the Urals, Yearbook-1988, Institute of Geology and Geochemistry. Uralian Branch of RAS, Sverdlovsk, 107-109. (In Russian)

Ronkin, YL, Poltavets, YA, Lepikhina, OP (1993) Isotope geochemical and structural characteristics of the location of large iron-ore skarn magnetite deposits: the Urals Russia. In: Short Papers – IV South American Symposium on Isotope Geology. 766-769.

Ronkin YL, Poltavets YA, Lepikhina OP, Poltavets ZI. 1997. Estimation of mantle and crustal material participation in evolution of huge Kachar ore-geochemical system of the Urals. Russia: Sr-Nd-Pb isotope limitations. In proc. 7th Annual VM goldscmidt conf. Abs. 2219.

Rosenbaum J, Sheppard SM. An isotopic study of siderites, dolomites and ankerites at high temperatures. Geochim. Cosmochim. Acta, 1986; 50:1147-1150.

Rye RO, Ohmoto H. Sulphur and Carbon isotopes and ore genesis: A review. Economic Geology. 1974; 68: 826-842.

Samarkin GI, Pumyanskiy, AM. 1983. The evolution of the Early Carboniferous magmatism of the Valeryanovo volcanic belt and its metallogeny, In: The geology and mineral raw-resources of the West Siberian Plate and its folded surroundings, Tyumen, 141-144. (In Russian).

Selby D, Creaser RA. Accurate and precise Re–Os molybdenite dates from the Galway Granite, Ireland. Critical comment on Disturbance of the Re–Os chronometer of molybdenites from the late-Caledonian Galway Granite, Ireland, by hydrothermal fluid circulation. Geochemical Journal, 2004; 38:291–294.

Selby D, Creaser RA. Re–Os geochronology and systematics in molybdenite from the Endako porphyry molybdenum deposit, British Columbia, Canada. Econ. Geol. 2001; 96:197–204.

Sharp ZD A laser-based microanalytical method for the insitu determination of oxygen isotope ratios of silicates and oxides. Geochim. Cosmochim. Acta, 1990; 54:1353-1357.

Sillitoe RH, Burrows DR. New field evidence bearing on the origin of the El Laco magnetite deposit, northern Chile: Econ. Geol. 2002; 97:1101-1109.

Sillitoe RH. Iron oxide-copper-gold deposits: an Andean view. Mineral. Dep. 2003; 38:787-812.

Smirnov, VI (ed.), 1977. Ore Deposits of the USSR Volume 1, Pitman Publishing, London, 7-113.

Smirnov VI, Dymkin AM. (eds.), 1989, Magnetite skarn deposits of the Urals: Central and southern Urals. Sverdlovsk: Uralian Branch Acad. Sci. USSR, 212 p. (in Russian).

Smith MP, Coppard J, Herrington R. Stein, H. The geology of the Rakkurijärvi Cu-(Au) prospect, Norrbotten: A new IOCG deposit in Northern Sweden. Econ. Geol. 2007; 102:393-414.

Smith MP, Gleeson, SA, Yardley, BWD (2013) Hydrothermal fluid evolution and metal transport in the Kiruna District, Sweden: Contrasting metal behaviour in aqueous and aqueous-carbonic brines. Geochimica et Cosmochimica Acta, 102, 89-112.

Sokolov GA. Grigorev VM. 1977. Deposits of Iron, In: Smirnov, V.I. (ed) Ore Deposits of the USSR Volume 1, Pitman Publishing, London, 7-113.

Sourirajan S. Kennedy GC. The system H_2O-NaCl at elevated temperatures and pressures. Amer. J. Sci. 1962; 260:115-141.

Sterner MS, Hall DL, Bodnar, RJ. 1987. Synthetic fluid inclusions. Solubility relations in the system NaCl-KCl-H_2O under vapor-saturated conditions. Geochim. Cosmochim. Acta, 1988; 52:989-1005.

Storey CD, Jeffries TE, Smith M. Common lead corrected laser ablation ICP-MS systematics and geochronology of titanite. Chem. Geol. 2006; 227:37-52.

Valley JW. Stable isotope geochemistry of metamorphic rocks . Rev. Mineral. 1986; 16: 445-489

Veizer J, Hoefs J. The nature of ^{18}O-^{16}O and ^{13}C-^{12}C secular trends in sedimentary carbonate rocks. Geochim. Cosmochim. Acta, 1976; 40:1387–1395.

Wang SQ, Williams P. (2001) Geochemistry and origin of Proterozoic skarns at the Mount Elliott Cu-Au(-Co-Ni) deposit, Cloncurry district, NW Queensland, Australia. Mineral. Dep. 2001; 36:109-124.

Webster, JD, Kinzler, RJ, Mathez, EA. 1998. Chloride and water solubility in basalt and andesite melts and implications for magmatic degassing Geochimica et Cosmochimica Acta, 63, 729–738

Williams CT. 1996. Analysis of rare earth minerals. In: Jones, A. P., Wall, F. & Williams, C. T. (eds) Rare Earth Minerals: Chemistry, Origin and Ore Deposits. London: Chapman & Hall, pp. 327-348.

Williams PJ, Barton MD, Johnson DA, Fontboté L, De Haller A, Mark G, Oliver NHS, Marschik R. 2005. Iron oxide-copper-gold deposits: Geology, space-time distribution, and possible modes of origin; In: Hedenquist, J.W., Thompson, J.F.H., Goldfarb, R.J. and Richards, J.P. (eds) Economic Geology, 100th Anniversary Volume, Society of Economic Geologists, 371-405.

Winter JD. 2001. An introduction to igneous and metamorphic petrology. Prentice-Hall, New Jersey. 796pp.

Yardley BWD. (2005) Metal concentrations in crustal fluids and their relationship to ore formation. Economic Geology, 100, 613-632.

Zackarov AM, Ksenofontov OS, Bekuhametov AE, Poltavets YA, Pumpyansky AM. 1987. Geology of the Turgai depression.In: Ovchinnikov, L.N. and Dymkin, A.M. (eds) Ore formations of the Urals, The Turgai depression, Sverdlovsk. (In Russian)

Zhang Z, Saxena SK. Thermodynamic properties of andradite and application to skarn with co-existing andradite and hedenbergite. Contrib. Mineral. Petrol. 1991; 107:255-263.

Zheng YF. Calculation of oxygen isotope fractionation in metal oxides. Geochim. Cosmochim. Acta, 1991; 55:2299-2307.

Zheng YF. Calculation of oxygen isotope fractionation in anhydrous silicate minerals. Geochim. Cosmochim. Acta, 1993a; 57:1079-1091.

Zheng YF. Calculation of oxygen isotope fractionation in hydroxyl-bearing silicates. Earth Planet. Sci. Lett., 1993b; 120:247-263.

Zonenshain LP, Korinevsky VG, Kazmin VG, Pechersky DM, Khain, VV, Matveenkov VV. Plate tectonic model of the South Urals Development. Tectonophysics, 1984; 109:95-135.

Figures

Figure 1: Simplified map showing the location of the Valerianovka arc, and tectonic sketch map of the southern Urals in Russia and Kazakhstan (after Brown et al., 2002; Herrington et al. 2002, 2005b), showing principle deposit localities. Shading of West Siberian Basin over the East Uralian Zone (notably at the Valerianovka Arc) indicates the continuation of the zone under Mesozoic cover.

Figure 2: Comparison of grade and tonnage in the Valerianovka deposits with major hydrothermal iron ores. Skarn related deposits are highlighted. Data on hydrothermal iron ores (IOA and IOCG related) from Williams et al. (2005). Data on Fe skarns from Meinert (1992).

Figure 3: The locations of the main deposits and magnetite occurrences of the Turgai belt in relation to the major intrusive series of theTransuralian zone, Faults = dashed red line. Deposits are confined to the Valerianovka zone (in green) between the Livanov and Apanov faults. Figure 4: Idealised stratigraphic column, showing the main units found in the Valerianovka zone. Black diamonds show where the Turgai iron skarns are hosted within the Sokolov Limestone (after Herrington et al., 2005a). Thicknesses shown are approximate and vary throughout the region.

Figure 5: Simplified plan maps of the A) Sokolov and B) Sarbai deposits. Adapted from Smirnov (1977). C) Plan map of the Kachar deposit (adapted from an anonymous mine map). Approximate line of sections in Figure 6 shown.

Figure 6: Geological cross sections through the main Turgai iron deposits. A) Kachar (adapted from Smirnov, 1977; B) Sokolov; C) Sarbai (B and C adapted from anonymous mine maps). The locations of the sections are shown on Figure 5.

Figure 7: Macroscale views of the geology of the Turgai skarns. A) View of the Sokolov open pit, looking WNW. The SSW dipping limestone and tuff sequence is visible, with the development of skarn (in limestone), magnetite, and Na-K alteration (In tuffs). B) View of the main ore zone, Sokolov open pit. Magnetite (Mgt) is developed at the contact between limestone and tuffs, with the development of andradite (And) and pyroxene-epidote skarn (Px-Ep). C) and D) Views of the Sarbai deposit showing the development of Na-K alteration in tuffs, and the post-ore dykes. The development of limestone bedding parallel magnetite layers is also visble in D.

Figure 8: Paragenetic sequence for the Turgai skarns derived from field and microscopic observations from this study. A) Sokolov; B) Sarbai, C) Kachar.

Figure 9: Primary appearance of host rocks. A) Contact metamorphosed limestone preserving symmetrical wave ripples, Sarbai. B) Nodular limestone, with an apparent chicken-wire texture, Sarbai. This rock is composed of calcite. C) Porphyritic dacite, Kachar. D) Coarse grained volcanic breccias (mapped as tuff), Sarbai.

Figure 10: Skarn type alteration in limestone from the Turgai skarns. (a) Back scattered electron (BSE) image showing quartz replacement of coral within limestone. Calcite is altered to a fine grained calcic amphibole rimmed in quartz. Sokholov.(b) Magnetite in fractures cutting pyroxene-epidote skarn. (c) Garnet+epidote+magnetite skarn, Sokolov. (d) BSE image showing garnet-diopside skarn overgrowing early amphibole, Sarbai. (e) BSE image showing magnetite intergrown with albite and apatite, Kachar. (f) BSE image showing magnetite-pyroxene-titanite skarn, brecciated and infilled with chorite and calcite intergrown with fine grained magnesian amphibole. Amph – amphibole; Cc – calcite; Qtz – quartz; Grt – garnet; Mgt – magnetite; Ep – epidote; Di – Dioside; Ttn – titanite; Chl – chlorite; Alb – albite; Ap – apatite.

Figure 11: Sulphide and suphate minerals in the Turgai skarns. (a) Pyrite-chalcopyrite-pyrrhotite in magnetite, Sarbai. (b) Massive pyrite and pyrrhotite enclosed by magnetite, Sarbai. (c) BSE image of Galena overgrowing and filling factures in pyrite, Kachar. (d) BSE image showing molybdenite and pyrite in interstices and fractures fills between epidote grains, Sarbai. (e) BSE image showing rounded pyrite bleb in magnetite, Kachar. (f) Calcite-K-feldspar vein with minor pyrite cutting magnetite, . (g) Gypsum vein cutting main skarn-stage minerals , Sarbai. (h) Cuprite and barite in fracture in magnetite, Kachar. Abbreviations as above, plus: Py – pyrite; Po – pyrrhotite; Mo – molybdenite; Gy – gypsum.

Figure 12: Development of the sulphide mineral assemblage, illustrated in reflected light. (a) Euhedral magnetite with later pyrite. (b) Co-exisitng magnetite, pyrite and chalcopyrite. (c) Magnetite and pyrite with subsequent hematite alteration of magnetite. (d) Coarse grained, platy hematite developed as replacement and overgrowth of magnetite. (e) Co-exsiting pyrite, pyrrhotite and magnetite, Sarbai. (f) Pyrrhotite inclusion in massive pyrite, Sarbai. (g) Magnetite and pyrite in fracture in pyrrhotite, Sarbai. (h) Chalcopyrite in fracture in pyrrhotite, Sarbai.

Figure 13: Sodic alteration. (a) Porphyritic metavolcanic, with albite-scapolite replacement of megacrysts, Kachar (b) Lithic breccias composed of volcanic clasts, some with complete replacement by magnetite, cemented by scapolite plus albite, Kachar. (c) Magnetite replacement of matrix around large (>1m) volcanic block in tuff/breccia, Sokolov. NB. Image is rotated 90°. (d) Sodic replacement of volcanic rocks. BSE image showing primary porphyry replaced by scapolite, albite and titanite, Kachar. (e) BSE image showing K-feldspar and actinolite replacing volcanic matrix around albite-altered phenocrysts, Kachar. (f) BSE image showing albite porphyroblasts developed in silicified marble distal to ore bodies. (Abbreviations as before, plus: Scp – scapolite; Ksp – K- feldspar; Cpy – chalcopyrite.

Figure 14: Replacement textures from the main magnetite ore zones. (a) Pyrite replacement along relict limestone laminae, now dominated by magnetite, Sarbai. (b), (c) Large magnetite ore blocks illustrating replacement of bivalves by pyroxene (b) and chalcopyrite (c). (d) Complete replacement of bivalve by magnetite, Sarbai. (e) Chalcopyrite replacement of Goniatite, cut slab ofmagnetite skarn, Sarbai. (f) Diopside replacing fossilised coral, encased within limestone replaced by magnetite, Kachar. Abbreviations as before.

Figure 15: Summary of mineral chemistry from Turgai skarns. (a) Pyroxene compoisition. (b) Garnet composition. (c) Calcite compositions. (d) Amphibole composition. (e) Scapolite composition. (f) Chlorite composition. (g) Temperatures calculated from chlorite IV site occupancy using the method of Cathelineau (1988).

Figure 16: Results of LA-ICPMS dating of titanite shown as Concordia plots and cumulative probability of age plots based on the $^{206}Pb/^{238}U$ age. (a)-(c) BSE images of titanite showing varying levels of hydrothermal alteration. (d) and e) Sample 68; Sarbai. (f) and g) Sample SOK3; Sokolovska. Data plotted using ISOPLOT 3.00 (Ludwig, 2003).

Figure 17: Results of stable isotope analyses. (a) Composition of major silicates and magnetite. (b) Results of $\delta^{18}O$ analyses of magnetite separated by deposit. (c) Results of $\delta^{34}S$ analyses of sulphides. (d) Results of $\delta^{34}S$ analyses of pyrite separated by deposit.

Figure 18: Fluid inclusion petrography. (a) Isolated group of inclusions in core of diopside crystal, sample 9, Kachar.(b) Lw+Sh+V inclusion in diopside, sample 9, Kachar.(c) Secondary trail of vapour dominated and Lw+V inc;usions in diopside, sample 9, Kachar. (d) Growth zone parallel band of inclusions in andradite, sample 23, Sokolov. (e) Inclusions along individual growth zones in andradite, sample 23, Sokolov. (f)+(g) Lw+Sh+V inclusion in andradite, sample 23, Sokolov. (h) Lw+V inclusions in calcite, sample 16, Kachar.

Figure 19: Results of preliminary analysis and interpretation of fluid inclusions from the Turgai skarns. (a) Salinity, determined from halite dissolution temperature, plotted against

homogenisation temperature. (b) Positions of representative isochors for the system NaCl-H_2O. Halite plus liquid plus vapour (HLV) curve (continuous line) based on the data of Sourirajan & Kennedy (1962). Halite liquidi for 50 and 35 wt % NaCl (L(50%); L(35%)) calculated from Bodnar (1994). Liquid-vapour curve [LV(50%)] taken from Chou (1987). Temperature ranges inferred from chlorite chemistry are shown for comparison.

Figure 20: Application of phase equilibria to constrain conditions of skarn formation. (a) T-XCO_2 section at 1kbar for the system NaCl-H_2O-CO_2 (Bowers and Helgeson, 1983). Below approximately 620ºC the fluid unmixes to a saline liquid plus CO_2-rich vapour. (b) T-XCO_2 section from 0-0.1 XCO_2, showing the principle pro-grade marble forming reactions. The dashed line shows the limit of the aqueous liquid phase composition of a, which constrains the fluid composition and hence the temperature of reactions (Winter, 2001). (c) T-fO_2 diagram constructed using SUPCRT92 (Johnson et al., 1992), using reactions from Zhang and Saxena (1991).

Figure 21: Interpretation of stable isotope data. (a) Results of calcite-magnetite and dioside-andradite O isotope geothermometry. (b) Interpretation of the carbon and oxygen stable isotope composition of carbonates in terms the interaction of magmatic-equilibrated fluids with marine limestone. Curves for the composition of calcite precipitated from such a fluid at varying XCO_2 calculated using the equation of Bowman (1998). Curves for the Rayleigh devolatilisation of calcite calculated using the equations of Valley (1986). Field for magmatic fluids from Bowman (1998), field for marine limestones for Veizer and Hoefs (1976). (c) Calculation of the composition of water in equilibrium with skarn silicates at a range of temperatures, compared with that of a range of potential crustal fluids. (d) Composition of Turgai skarn sulphide and sulphate $\delta^{34}S$ with the composition of major earth reservoirs (Ohmoto and Rye, 1979). See text for discussion.

Figure 22: Comparison of the age of recognised tectonic events in the southern Urals with the age of magnetite mineralisation in the Magnitogorsk and Valerianovska zones, and the age of a range of related intrusive suites.

Tables

Table 1: Representative analyses of silicate minerals from Turgai skarns. OH and CO_3 in amphibole and scapolite determined by difference. FeII and FeIII in amphibole estimated using the method of Leake et al. (1997). ND - not detected.

Table 2: Representative analyses of chlorite from the Turgai skarns, with temperatures calculated using the equation of Cathelineau (1988).

Table 3: Representative analyses of calcite from Turgai skarn and veins.

Table 4: Results of Re/Os dating of molybdenite from Sarbai sample SARB6. TC Os = Total common osmium.

Table 5: Results of common Pb corrected LA_ICPMS U-Pb isotope analyses of titanite.

Table 6: Results of stable isotope analyses of silicates, calcite and sulphides. Oxygen analyses presented relative to SMOW, carbon analyses relative to PDB and sulphur analyses relative to CDT. Mag - magnetite; Hem - hematite; Pyx - diopside pyroxene; Epi - epidote; Grt - garnet; Cal - calcite; Py - pyrite; Po - pyrrhotite; Cpy - chalcopyrite; Gyp - gypsum.

Table 7: Results of fluid inclusion analyses. Tm - ice melting temperature; T_h solid - solid phase homogenisation, usually halite dissolution; T_h (L-V) - total homogenisation to liquid phase.

Table 1: Representative analyses of silicate minerals from Turgai skarns. OH and CO3 in amphibole and scapolite determined by difference. FeII and FeIII in amphibole estimated using the method of Leake et al. (1997). ND - not detected. #Sok. – Sokholov.

	Pyroxene				Garnet				Amphibole				Scapolite		
	Sarbai	Kachar	Sok.#		Sarbai	Kachar	Sok.#		Sarbai	Kachar	Sok.#		Kachar	Kachar	Kachar
Na2O	0.63	0.43	0.22	Na2O	0.01	0.01	0.06	Na2O	0.16	0.52	0.36	Na2O	4.96	9.48	10.70
K2O	0.00	0.06	0.02	K2O	ND	ND	0.01	K2O	0.08	0.00	0.00	K2O	1.03	1.35	0.70
CaO	23.60	24.86	24.95	CaO	33.76	33.17	23.21	CaO	12.60	13.94	12.27	CaO	4.63	3.73	2.92
MgO	13.09	13.47	14.84	MgO	0.19	0.25	0.03	MgO	15.40	18.28	16.61	MgO	0.01	0.01	0.00
MnO	0.29	0.32	0.62	MnO	1.38	0.43	0.39	MnO	0.31	0.33	0.14	FeO	0.28	0.22	0.20
FeO	7.94	7.13	5.08	Fe2O3	15.07	24.67	15.42	FeO	10.87	5.39	8.71	Al2O3	22.95	24.31	23.89
Al2O3	1.63	2.81	0.35	Al2O3	11.98	5.15	22.45	Fe2O3	3.00	4.72	2.01	SiO2	61.45	58.27	62.25
SiO2	51.58	50.53	53.38	SiO2	37.3	36.06	38.2	Al2O3	2.51	6.16	2.20	SO3	ND	ND	ND
TiO2	0.14	0.24	0.01	TiO2	0.56	0.66	0.01	SiO2	53.49	46.89	53.10	Cl	3.83	2.70	1.56
Cr2O3	ND	0.01	0.05	Cr2O3	0.03	0.02	0.00	TiO2	0.06	0.11	0.22	F	ND	ND	ND
								Cr2O3	0.00	0.01	0.01	Total	99.19	100.09	102.27
								H2O	4.07	3.97	4.16	Cl = 0	0.86	0.61	0.35
Total	98.90	99.86	99.28	Total	98.78	97.94	98.23	Total	102.55	100.32	99.79	Total	98.24	99.48	101.92
Formulae to	**6 (O)**				**12 (O)**				**23 (O, OH)**				**12 (Si, Al)**		
Na	0.047	0.031	0.016	Na	0.002	0.002	0.009	Na	0.044	0.145	0.101	Na	1.303	2.535	2.750
K	0.000	0.003	0.001	K	0.000	0.000	0.001	K	0.015	0.000	0.000	K	0.179	0.238	0.119
Ca	0.953	0.999	0.994	Ca	2.871	2.916	1.880	Ca	1.925	2.158	1.906	Ca	0.673	0.552	0.415
Mg	0.745	0.758	0.827	Mg	0.023	0.031	0.003	Mg	3.294	3.962	3.612	Mg	0.002	0.002	0.000
Mn	0.008	0.010	0.019	Mn	0.093	0.030	0.025	Mn	0.037	0.040	0.017	Fe	0.032	0.025	0.022
Fe	0.246	0.223	0.157	Fe	0.897	1.518	0.875	Fe	1.613	1.161	1.271	Al	3.658	3.951	3.733
Al	0.075	0.124	0.015	Al	1.119	0.497	1.997	FeIII	0.401	0.914	0.265	Si	8.342	8.049	8.267
Si	1.952	1.896	1.984	Si	2.960	2.958	2.889	Al	0.421	1.047	0.375	S	0.000	0.000	0.000
Ti	0.004	0.007	0.000	Ti	0.068	0.082	0.001	Si	7.628	6.776	7.699	Cl	0.879	0.630	0.350
Cr	0.000	0.000	0.001	Cr	0.002	0.001	0.000	Ti	0.006	0.012	0.024	F	0.000	0.000	0.000
								Cr	0.000	0.001	0.001	CO3	0.121	0.370	0.650
								OH	2.000	2.000	2.000				

Table 2: Representative analyses of chlorite from the Turgai skarns, with temperatures calculated using the equation of Cathelineau (1988).

	Kachar	Kachar	Kachar	Kachar	Sarbai	Sok.#	Sok.#	Sok.#
Na2O	0.06	0.02	0.06	0.03	0.01	ND	0.04	0.01
K2O	ND	0.06	0.08	ND	ND	ND	ND	0.02
CaO	0.37	0.22	0.25	0.11	0.06	0.05	0.05	0.07
MgO	24.3	17.26	19.23	21.02	19.14	16.03	14.81	21.02
MnO	0.34	0.17	0.2	0.91	0.15	0.18	0.76	0.10
FeO	12.3	20.48	21.45	17.12	20.81	19.66	24.65	18.28
TiO2	0.01	0.03	0.04	0.02	0.02	ND	0.01	ND
Cr2O3	ND	0.03	0.02	0.03	ND	ND	ND	ND
Al2O3	13.5	14.01	14.53	18.16	19.55	16.61	18.90	17.96
SiO2	36.68	35.93	32.29	29.08	28.21	35.68	27.37	25.76
F	ND	ND	ND	ND	ND	ND	ND	ND
Cl	ND	0.04	0.05	ND	ND	ND	ND	ND
H2O*	13.27	12.71	12.48	12.73	12.54	12.87	12.21	12.57
Total	100.83	100.96	100.68	99.21	100.49	101.08	98.80	95.80
O=Cl		0.02	0.02					
Total	100.83	100.94	100.66	99.21	100.49	101.08	98.80	95.80
Formulae to 28 (O, OH)								
Na	0.022	0.008	0.024	0.012	0.004	0.000	0.016	0.006
K	0.000	0.015	0.021	0.000	0.000		0.000	0.007
Ca	0.077	0.047	0.055	0.024	0.013	0.011	0.011	0.016
Mg	7.056	5.175	5.869	6.445	5.859	4.765	4.727	6.782
Mn	0.056	0.029	0.034	0.157	0.026	0.030	0.137	0.019
Fe	1.984	3.411	3.637	2.916	3.539	3.247	4.371	3.278
Ti	0.001	0.004	0.006	0.003	0.003	0.000	0.002	0.000
Cr	0.000	0.005	0.003	0.005	0.000	0.000	0.000	
Al	3.075	3.294	3.478	4.367	4.694	3.872	4.731	4.547
Si	7.101	7.181	6.570	5.944	5.757	7.070	5.823	5.541
F	0.000	0.000	0.000	0.000	0.000	0.000	0.000	0.000
Cl	0.000	0.027	0.034	0.000	0.000	0.000	0.000	0.000
OH*	8.000	7.973	7.966	8.000	8.000	8.000	8.000	8.000
T (ºC)	83	70	168	269	299	88	288	334

* H2O and OH determined by difference.

Sokholov

Table 3: Representative analyses of calcite from Turgai skarn and veins.

	Kachar	Kachar	Kachar	Sarbai	Sarbai	Sarbai	Sok.#	Sok.#	Sok.#
Na2O	0.68	ND	0.05	ND	0.03	ND	ND	0.03	ND
K2O	ND	ND	ND	ND	0.27	ND	ND	ND	ND
CaO	48.73	51.63	53.25	49.26	53.04	53.72	54.19	54.67	57.69
MgO	0.03	0.02	0.92	0.86	1.35	0.01	0.29	0.07	0.02
MnO	0.07	0.03	0.17	0.2	0.16	0.01	0.11	0.05	0.12
FeO	2.16	0.07	1.69	1.28	0.39	0.19	0.15	0.14	1.35
NiO	ND	ND	0.03	ND	ND	ND	0.01	ND	ND
Cr2O3	ND	0.01	ND	ND	ND	ND	ND	0.01	ND
TiO2	0.01	0.02	ND	0.01	0.03	ND	0.01	0.02	ND
Al2O3	ND	ND	0.02	0.01	0.3	ND	ND	ND	ND
SiO2	0.15	2.68	0.22	0.02	1.24	0.26	0.03	0	0.02
CO2*	43.80	45.03	44.06	44.02	44.68	44.08	44.04	44.00	43.87
Total	95.63	99.49	100.41	95.66	101.49	98.27	98.83	98.99	103.07
Formulae to 1 (CO3)									
Na	0.024	0.000	0.002	0.000	0.001	0.000	0.000	0.001	0.000
K	0.000	0.000	0.000	0.000	0.006	0.000	0.000	0.000	0.000
Ca	0.948	0.909	0.943	0.953	0.908	0.988	0.987	0.994	0.979
Mg	0.001	0.000	0.023	0.023	0.032	0.000	0.007	0.002	0.000
Mn	0.001	0.000	0.002	0.003	0.002	0.000	0.002	0.001	0.002
Fe	0.033	0.001	0.023	0.019	0.005	0.003	0.002	0.002	0.018
Ni	0.000	0.000	0.000	0.000	0.000	0.000	0.000	0.000	0.000
Cr	0.000	0.000	0.000	0.000	0.000	0.000	0.000	0.000	0.000
Ti	0.000	0.000	0.000	0.000	0.000	0.000	0.000	0.000	0.000
Al	0.000	0.000	0.000	0.000	0.006	0.000	0.000	0.000	0.000
Si	0.003	0.044	0.004	0.000	0.020	0.004	0.001	0.000	0.000
CO3	1.000	1.000	1.000	1.000	1.000	1.000	1.000	1.000	1.000

*CO3 and CO2 determined by charge balance.
#Sokholov

Table 4: Results of Re/Os dating of molybdenite from Sarbai sample SARB6. TC Os = Total common osmium.

Sample	Re (ppm)	± 2σ	187Re (ppb)	± 2σ	187Os (ppb)	± 2σ	TC Os (ppb)	Model Age (Ma)	± 2σ
Run 1	3.033	0.007	1906	5	10.71	0.01	29.3	336.2	1.3
Run 2	3.162	0.008	1987	5	11.13	0.01	32.4	335.2	1.3

Table 5: Results of common Pb corrected LA_ICPMS U-Pb isotope analyses of titanite.

Sample/ analysis no.	$^{207}Pb/^{235}U$	2σ	Age	2σ	$^{206}Pb/^{238}U$	2σ	Age	2σ
68 (Sokolhov)								
no12c05	0.3335	0.03355	292	51	0.0554	0.00227	347	28
no12c06	0.3847	0.02531	330	37	0.0547	0.0009	343	11
no12c07	0.4105	0.03222	349	46	0.0504	0.0008	317	10
no12c08	0.3781	0.01925	326	28	0.0515	0.00103	324	13
no12c09	0.3795	0.01472	327	22	0.0521	0.00092	327	11
no12c10	0.3793	0.01271	326	19	0.052	0.00064	327	8
no12c11	0.4338	0.03913	366	55	0.0541	0.00121	340	15
no12c12	0.4193	0.03287	356	47	0.0512	0.00101	322	12
no12c13	0.3763	0.02066	324	31	0.0523	0.00087	329	11
no12c14	0.3755	0.01506	324	22	0.0522	0.00098	328	12
no12c15	0.4078	0.05277	347	76	0.0536	0.00105	337	13
no12c16	0.464	0.01564	387	22	0.0526	0.00132	331	16
no12d05	0.524	0.03511	428	47	0.0556	0.00151	349	18
no12d06	0.3601	0.02319	312	35	0.0512	0.00182	322	22
no12d07	0.3863	0.01839	332	27	0.052	0.00067	327	8
no12d08	0.311	0.0246	275	38	0.0538	0.00284	338	35
no12d09	0.3803	0.01487	327	22	0.0507	0.00084	319	10
no12d10	0.3778	0.01844	325	27	0.0523	0.0011	329	13
no12d11	0.4044	0.01933	345	28	0.0505	0.00065	317	8
no12d12	0.3868	0.02332	332	34	0.0514	0.00101	323	12
no12d13	0.3789	0.02626	326	39	0.0532	0.00077	334	9
no12d14	0.3814	0.03372	328	50	0.0505	0.0018	318	22
no12d15	0.3902	0.03863	335	56	0.0519	0.00174	326	21
no12d16	0.3863	0.04412	332	65	0.0536	0.00176	337	21
SOK3 (Sokolhov)								
no11a05	0.3528	0.01697	307	25	0.0507	0.00163	319	20
no11a06	0.3494	0.01265	304	19	0.0466	0.00091	294	11
no11a07	1.0086	0.0353	708	36	0.0529	0.00137	332	17
no11a08	0.334	0.00975	293	15	0.0469	0.00087	296	11
no11a09	0.3261	0.00799	287	12	0.0438	0.00071	276	9
no11a10	0.3967	0.01829	339	27	0.0475	0.0007	299	9
no11a11	0.3922	0.02134	336	31	0.0468	0.00197	295	24
no11a12	0.4226	0.02882	358	41	0.05	0.00107	314	13
no11a13	0.3246	0.01558	285	24	0.0486	0.00134	306	16
no11a14	0.3602	0.01091	312	16	0.0473	0.00083	298	10
no11a15	0.3939	0.00961	337	14	0.0485	0.00048	305	6
no11a16	0.4037	0.00949	344	14	0.0497	0.00056	312	7
no12a05	0.3902	0.00976	304	11	0.0484	0.00088	334	14
no12a06	1.232	0.05285	356	14	0.0568	0.00118	815	48
no12a07	0.3303	0.00628	297	5	0.0471	0.00041	290	10
no12a08	0.3624	0.01207	297	13	0.0472	0.00106	314	18
no12a09	0.3588	0.01209	297	9	0.0472	0.00077	311	18
no12a10	2.3274	0.0782	392	22	0.0627	0.00184	1221	48
no12a11	0.3853	0.01507	320	9	0.0509	0.00075	331	22
no12a12	0.4893	0.0162	318	10	0.0506	0.00083	404	22

Table 5 (Cont.): Results of common Pb corrected LA_ICPMS U-Pb isotope analyses of titanite.

Sample/ analysis no.	$^{207}Pb/^{235}U$	2σ	Age	2σ	$^{206}Pb/^{238}U$	2σ	Age	2σ
no12a13	0.4337	0.01496	304	7	0.0483	0.00058	366	21
no12a14	0.3457	0.01614	297	6	0.0472	0.00051	302	24
no12a15	0.5936	0.01591	310	10	0.0493	0.00084	473	20
no12a16	0.3902	0.02049	310	15	0.0493	0.00125	335	30
no12b05	0.3701	0.01014	320	15	0.0473	0.00091	298	11
no12b06	0.3563	0.01571	309	24	0.0488	0.00068	307	8
no12b07	0.4113	0.01501	350	22	0.0468	0.00094	295	12
no12b08	0.3874	0.01457	332	21	0.0458	0.00144	289	18
no12b09	0.3639	0.01077	315	16	0.0476	0.00074	300	9
no12b10	0.752	0.03858	569	45	0.0538	0.00049	338	6
no12b11	0.4032	0.01895	344	27	0.0489	0.00099	308	12
no12b12	0.7168	0.02903	549	34	0.0504	0.00066	317	8
no12b13	0.3663	0.00696	317	10	0.0461	0.00064	290	8
no12b14	0.4082	0.01339	348	19	0.0484	0.0009	305	11
no12b15	0.354	0.00797	308	12	0.0487	0.00055	306	7
no12b16	0.8911	0.04767	647	51	0.0521	0.00094	327	11
no13a05	0.4457	0.01783	374	25	0.0496	0.001	312	12
no13a06	0.4085	0.0098	348	14	0.0461	0.00033	290	4
no13a07	0.3415	0.00645	298	10	0.0472	0.00045	297	6
no13a08	0.4202	0.0092	356	13	0.0503	0.00057	316	7
no13a09	0.4541	0.01608	380	22	0.0526	0.00103	331	13
no13a10	0.4414	0.00724	371	10	0.0471	0.00049	297	6
no13a11	0.7546	0.01879	571	22	0.0479	0.00091	302	11
no13a12	0.3231	0.01053	284	16	0.0454	0.00049	286	6
no13a13	0.6184	0.01497	489	19	0.0466	0.00057	294	7
no13a14	0.3824	0.02317	329	34	0.0447	0.00065	282	8
no13a15	0.4613	0.01591	385	22	0.0466	0.00058	294	7
no13a16	0.3626	0.01889	314	28	0.044	0.00044	278	5

Table 6: Results of stable isotope analyses of silicates, calcite and sulphides. All values in ‰. Oxygen analyses presented relative to SMOW, carbon analyses relative to PDB and sulphur analyses relative to CDT.

Sample No.	Deposit	$\delta^{18}O$						$\delta^{13}C$	$\delta^{34}S$			
		Mag	Hem	Pyx	Epi	Grt	Cal	Cal	Py	Po	Cpy	Gyp
13	Kachar	7.3					18.9	-10.8				
16		2.1					22.1	-9.2				
30			-1.0	5.3					-3.3			
53		5.1					19.9	-9.4				
58		3.2										
13c							18.0	-10.0				
48-K4		9.1										
KACH-10		2.7										
VAR-K-03							23.0	-7.0				
VAR-K-04									1.4			
VAR-K-05							23.4	-9.6	0.5			
VAR-K-06							19.9	-8.9				
VARK3		4.6					16.0	-2.7	0.4			
VAR-K-8		3.5										
VAR-KA-04		3.3					19.5	2.9	0.3			
VAR-KA-04									-0.3			
VAR-KA-05			-2.7									
VAR-KA-06							14.4	1.5				
6		2.9		8.6								
27		2.7		5.0								
20							14.1	-0.9				
55		-1.5					14.0	-2.4	1.7			
1	Sarbai								-1.5	0.1		
2									-2.7			
25									-0.9	6.6		
26												
33							14.4	-3.7	1.1			
43									-1.8			
28									0.9			
45-SR5					3.9							
SARB6												
SARB7							5.5	-14.0				
VARB4							15.6	-0.8				
VARB6									-1.2			9.6
VARB7		6.0			8.1		20.7	-12.1				12.9
VARB 8												4.9
VARB9		5.6					14.8	-4.4				
VAR-S-01							15.9	-1.9				
VAR-SA-01				9.4								
VAR-SA-02									0.3	-0.9	4.4	
VAR-SA-03									-3.8			
VAR-SA-04		7.4			8.1							
12							26.2	-2.7				

Mag - magnetite; Hem - hematite; Pyx - diopside pyroxene; Epi - epidote; Grt - garnet; Cal - calcite; Py - pyrite; Po - pyrrhotite; Cpy - chalcopyrite; Gyp - gypsum.

Table 6 (cont.): Results of stable isotope analyses of silicates, calcite and sulphides. All values in ‰. Oxygen analyses presented relative to SMOW, carbon analyses relative to PDB and sulphur analyses relative to CDT.

Sample No.	Deposit	$\delta^{18}O$						$\delta^{13}C$	$\delta^{34}S$			
		Mag	Hem	Pyx	Epi	Grt	Cal	Cal	Py	Po	Cpy	Gyp
22-SK2	Sokolov	3.5		4.3	7.5							
41-SK6				4.7	6.6							
52 SK7		0.4										
SOK					6.2							
VAR-SO-02		1.1					14.0	-4.0	1.4			
VAR-SO-04		2.8		5.2								
VAR-SOB-3		2.7		7.8	6.8	6.0						
VAR-SOB-4		2.3		6.1	5.2	6.3			2.8			
21		3.4			6.9							
24 - SOK									1.9			
24- SOK (2)									0.5			
SOK - 2							14.0	-4.4	2			
SOK - 4		1.6							1.9			
SOK- 2							13.7	-4.0				
VAR-SK-01							13.9	-4.2	1.6			
VAR-SK-01									1.4			
23		3.4			6.5	6.3						
42									-2.7			
VAR-SOB-1							20.6	1.7				

Mag - magnetite; Hem - hematite; Pyx - diopside pyroxene; Epi - epidote; Grt - garnet; Cal - calcite; Py - pyrite; Po - pyrrhotite; Cpy - chalcopyrite; Gyp - gypsum.

Table 7: Results of fluid inclusion analyses. Tm - ice melting temperature; Th solid - solid phase homogenisation, usually halite dissolution; Th (L-V) - total homogenisation to liquid phase.

Sample	Mineral	FI type	$T_m$ice	T_h solid	Wt% NaCl	T_h (L-V)
16	Calcite 1.	Lw+V	-19		21.7	137
		Lw+V	-21		23	117
		Lw+V	-17		20.2	130
		Lw+V	-20		22.4	142
		Lw+V	-25		23.2	301
68	Calcite	Lw+V	-20		22.4	385
27	Pyroxene	Lw+Sh+V		276	36.4	296
9	Pyroxene	Lw+Sh+V		400	47.4	600
		Lw+Sh+V	-70	420	49.7	600
		Lw+Sh+V			50.6	600
		Lw+Sh+V		415	49.1	598
23	Garnet	Lw+Sh+V		240	34.1	280

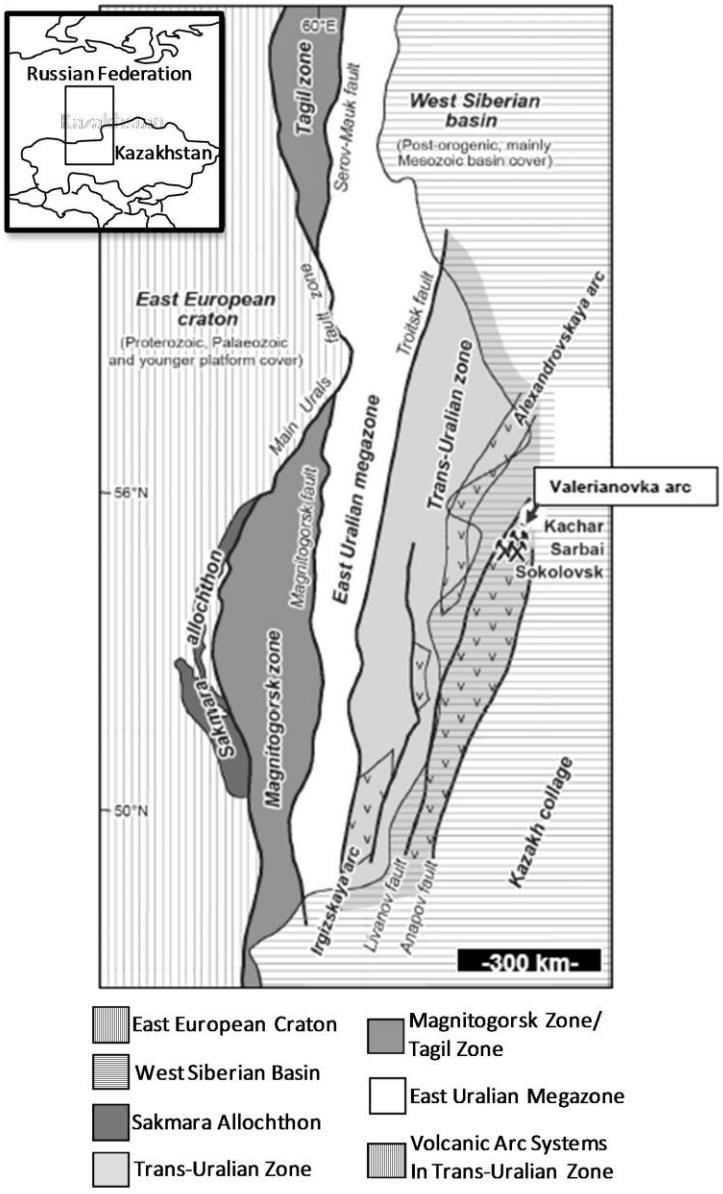

Figure 1

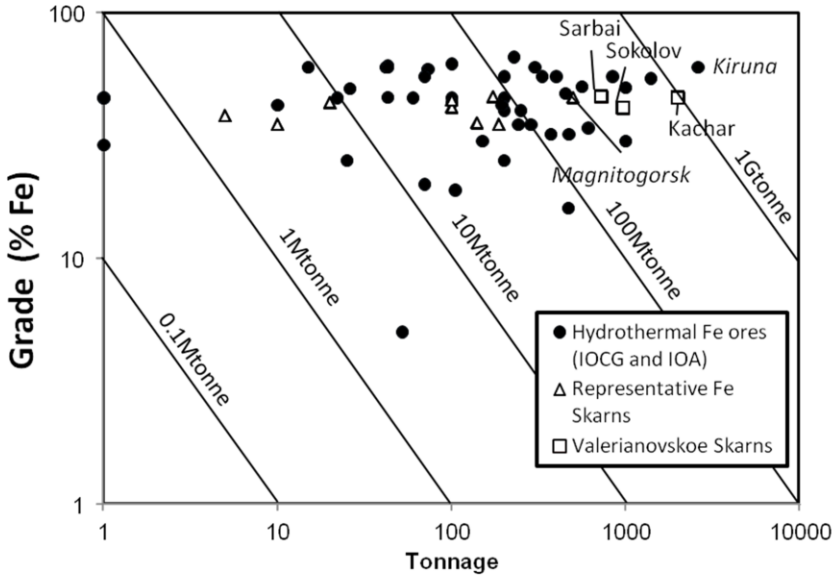

Figure 2

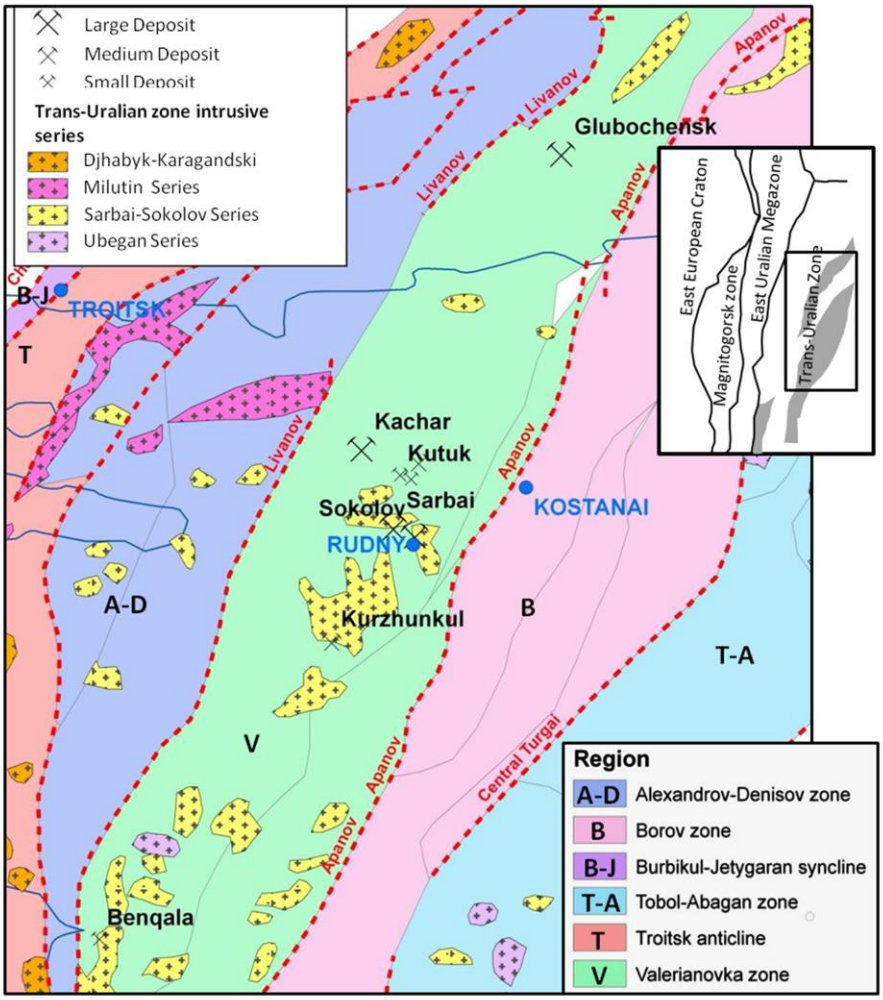

Figure 3

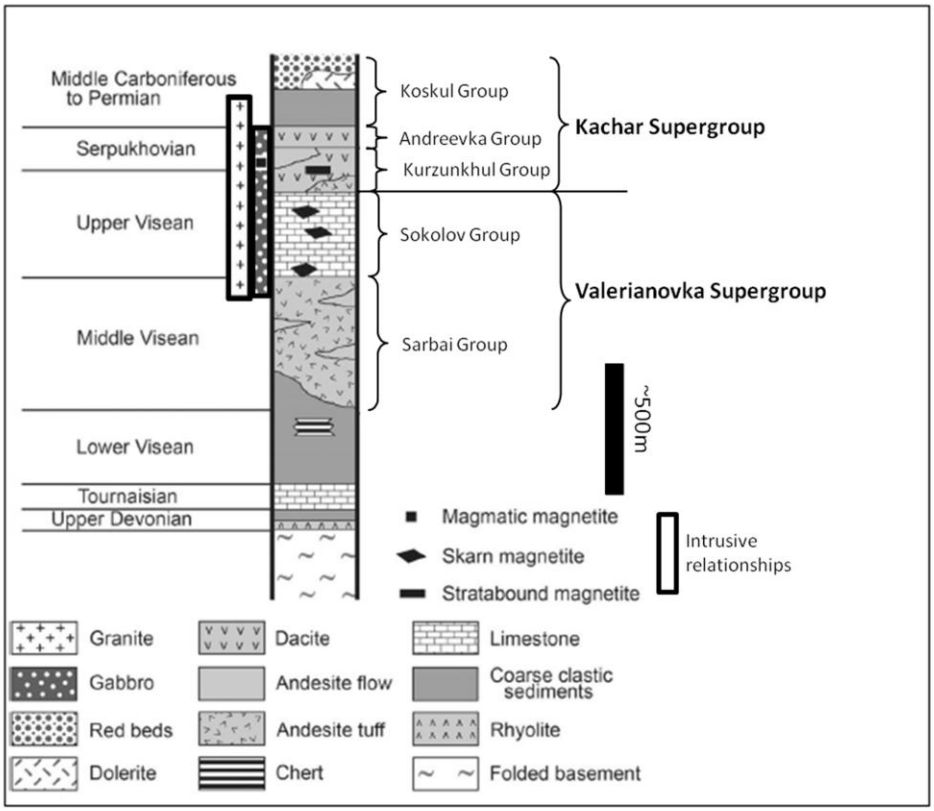

Figure 4

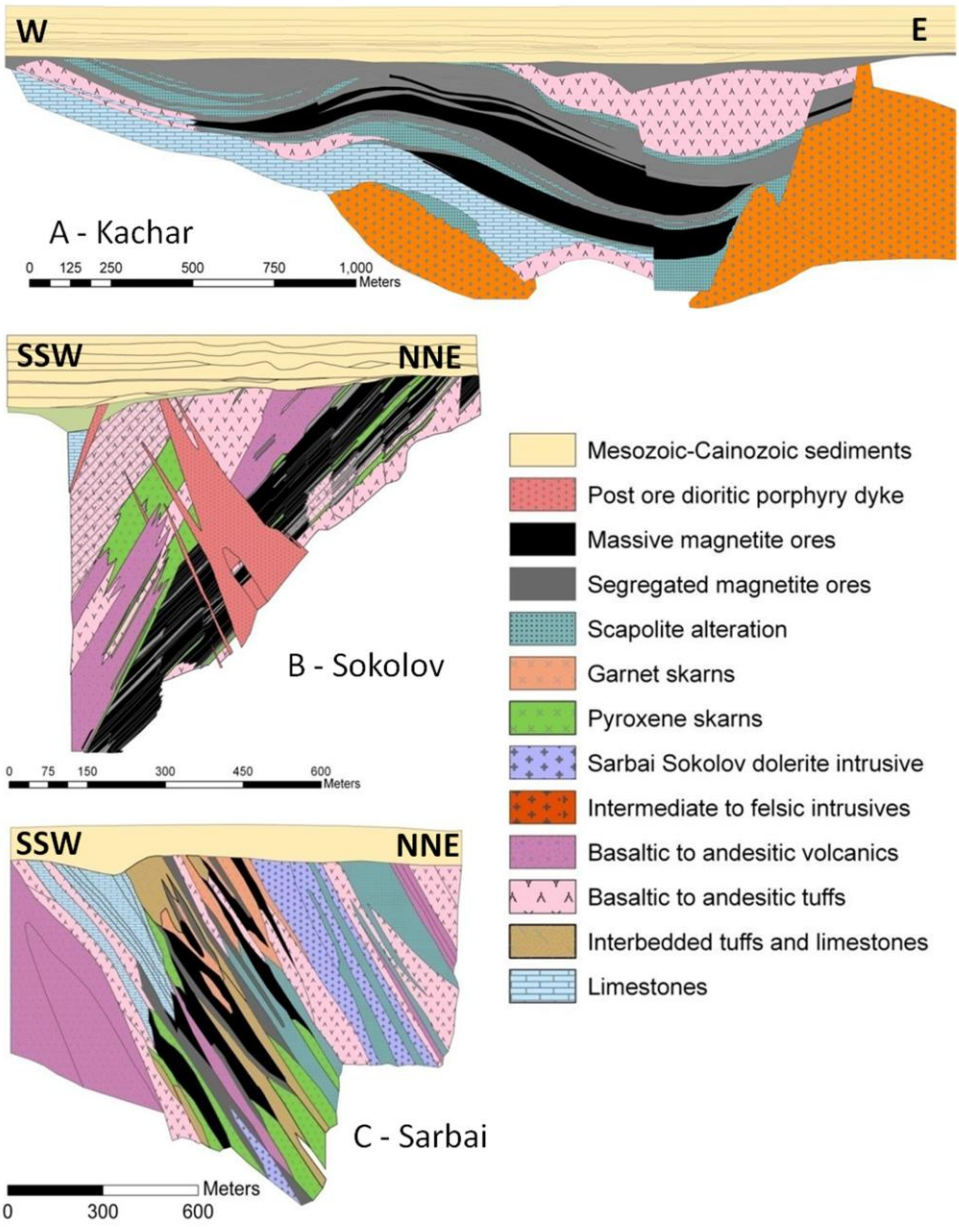

Figure 6

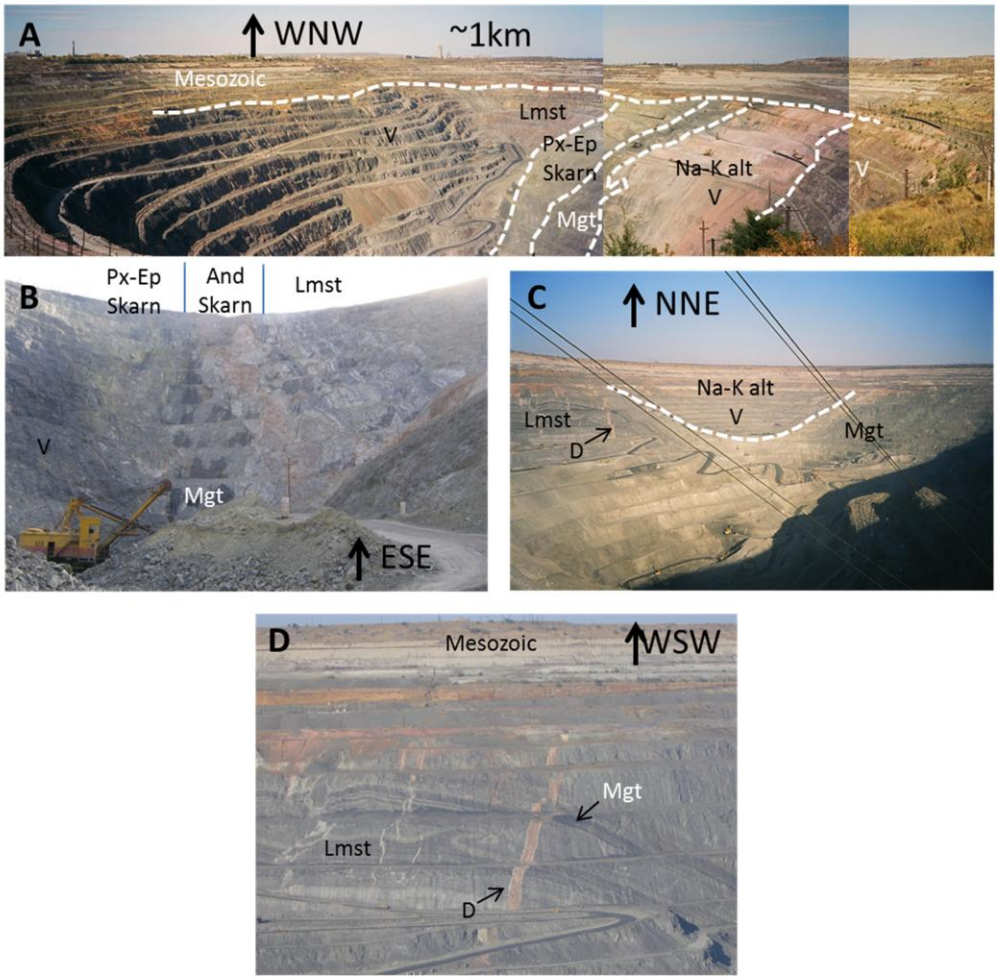

Figure 7

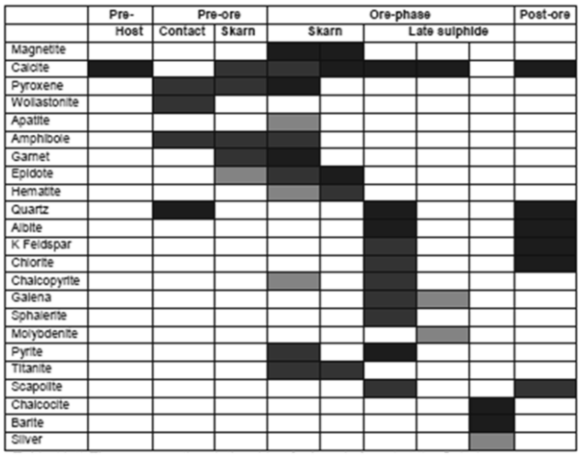

A) Sokolov

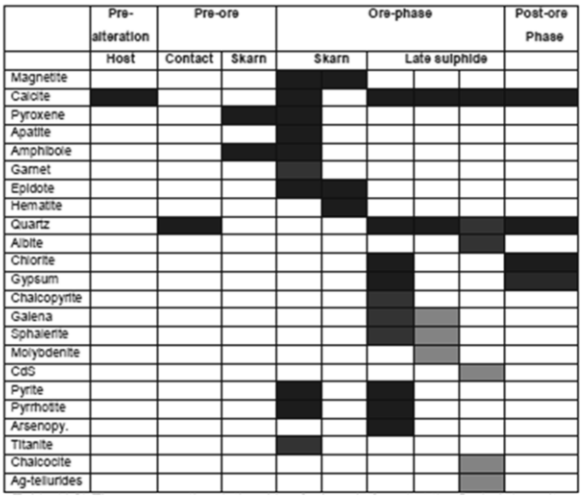

B) Sarbai

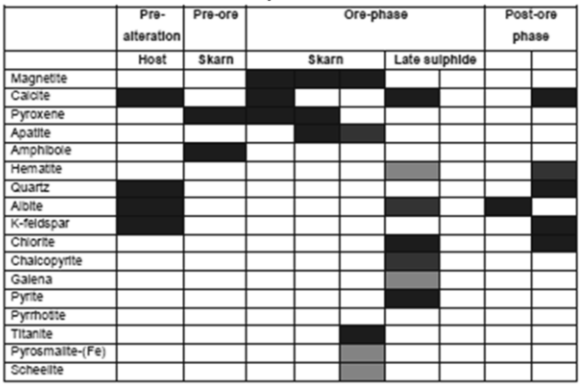

C) Kachar

Figure 8

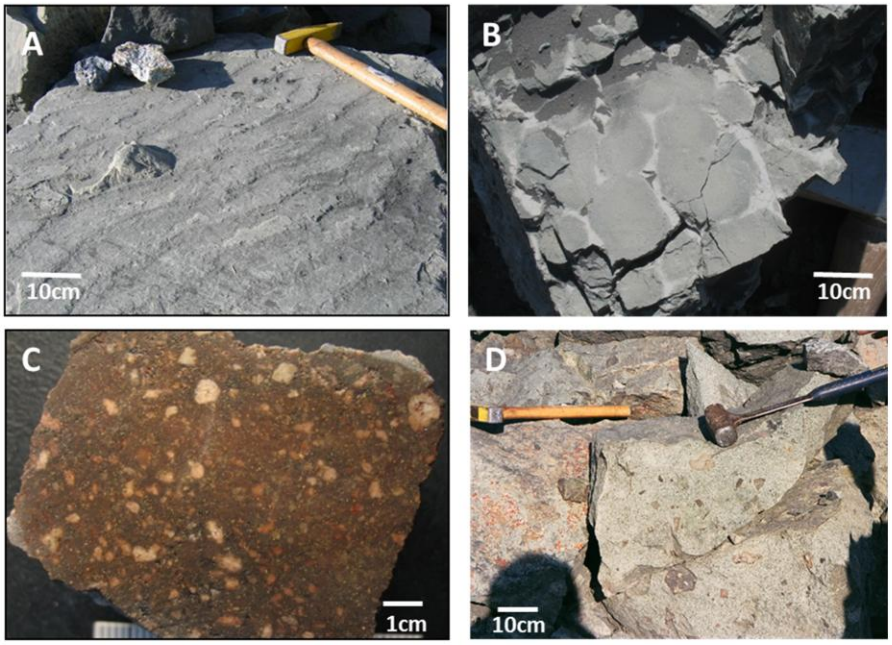

Figure 9

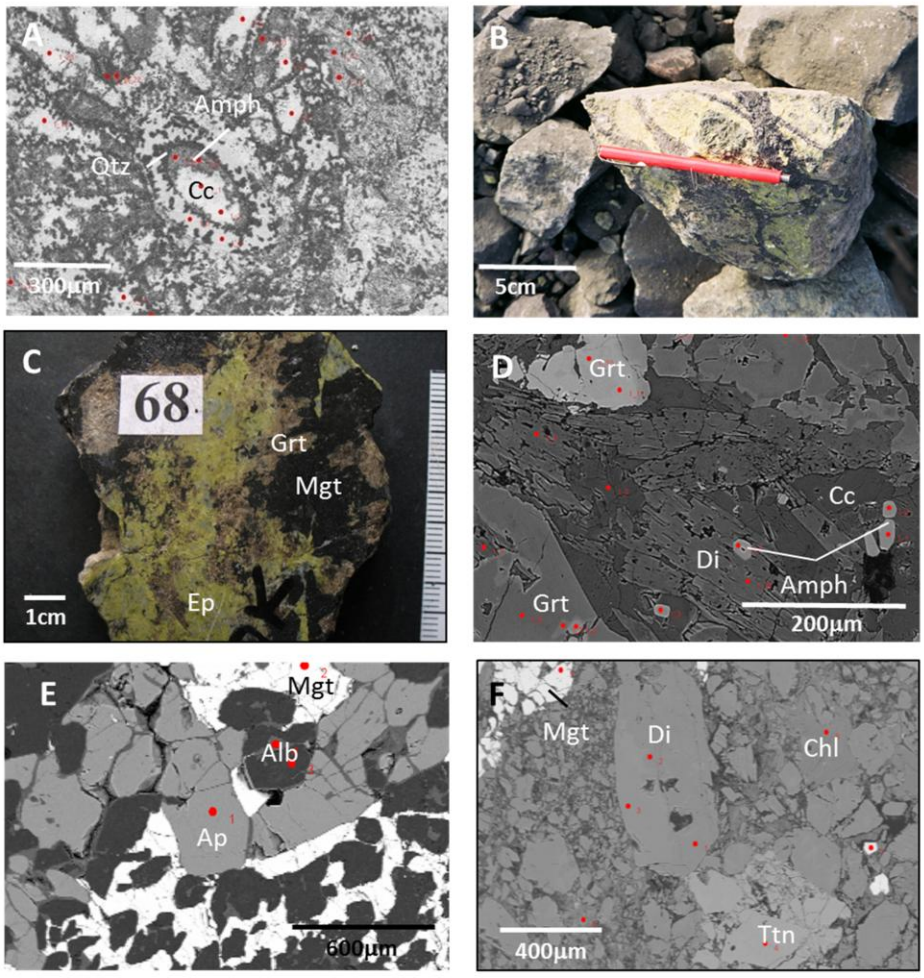

Figure 10

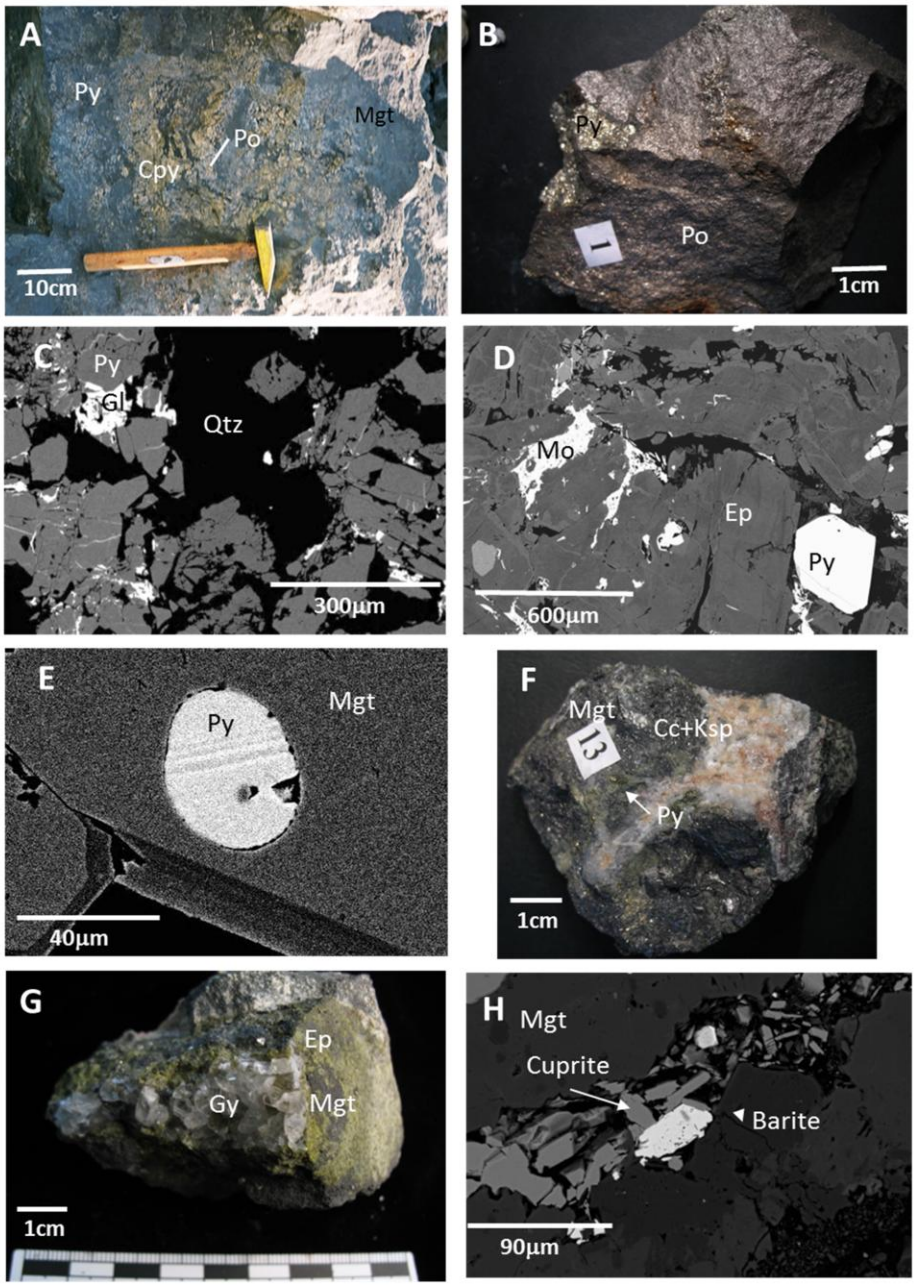

Figure 11

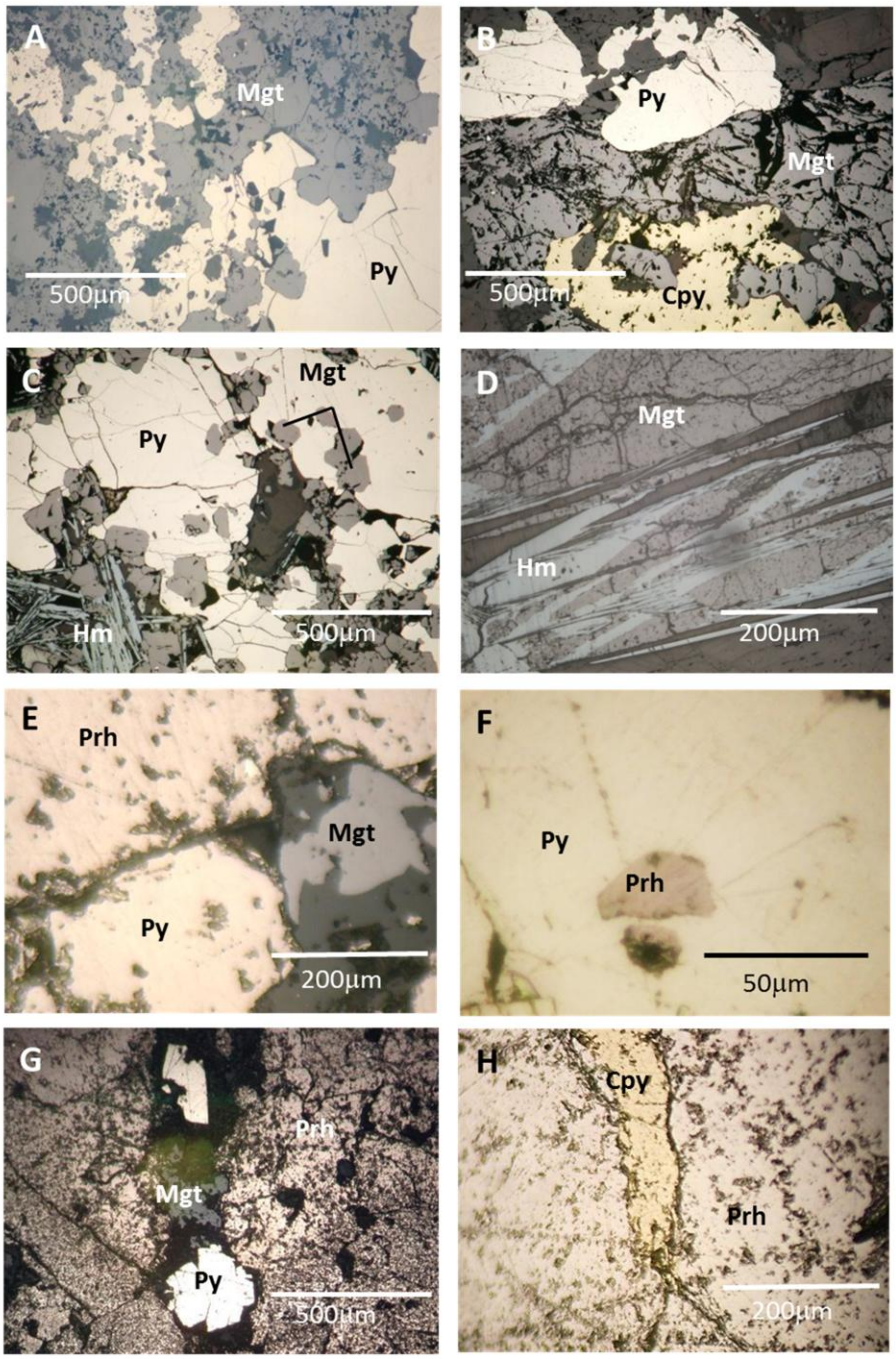

Figure 12

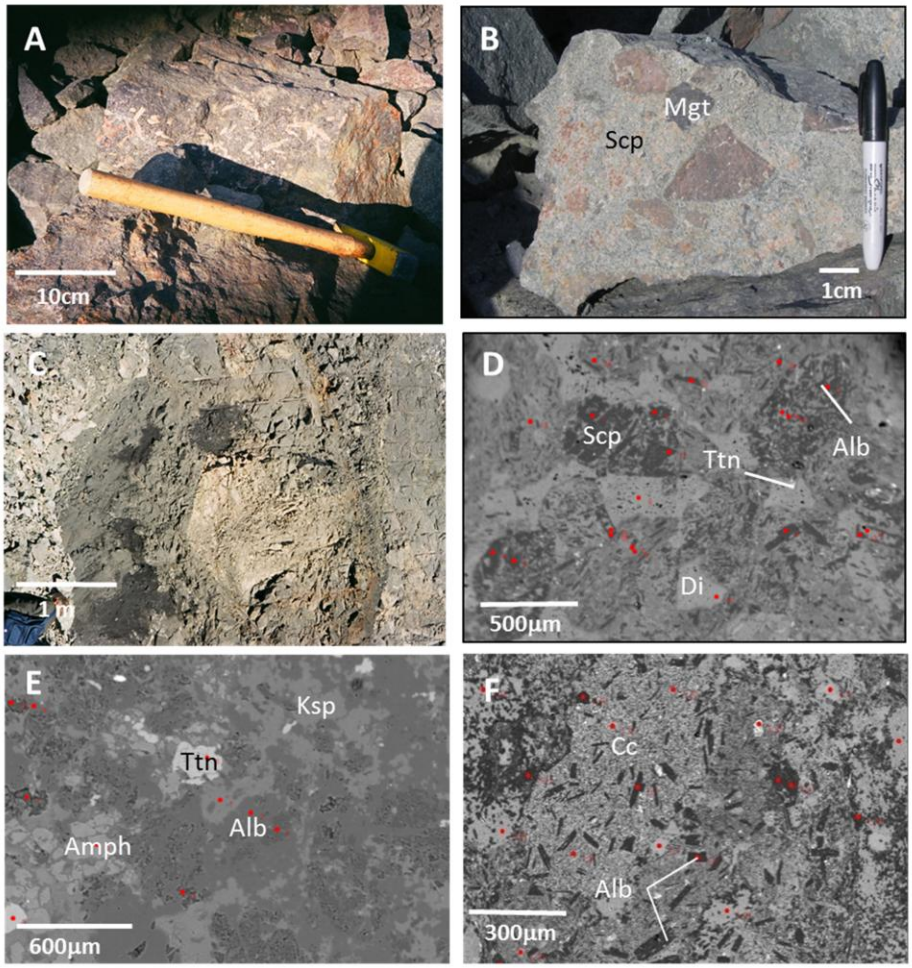

Figure 13

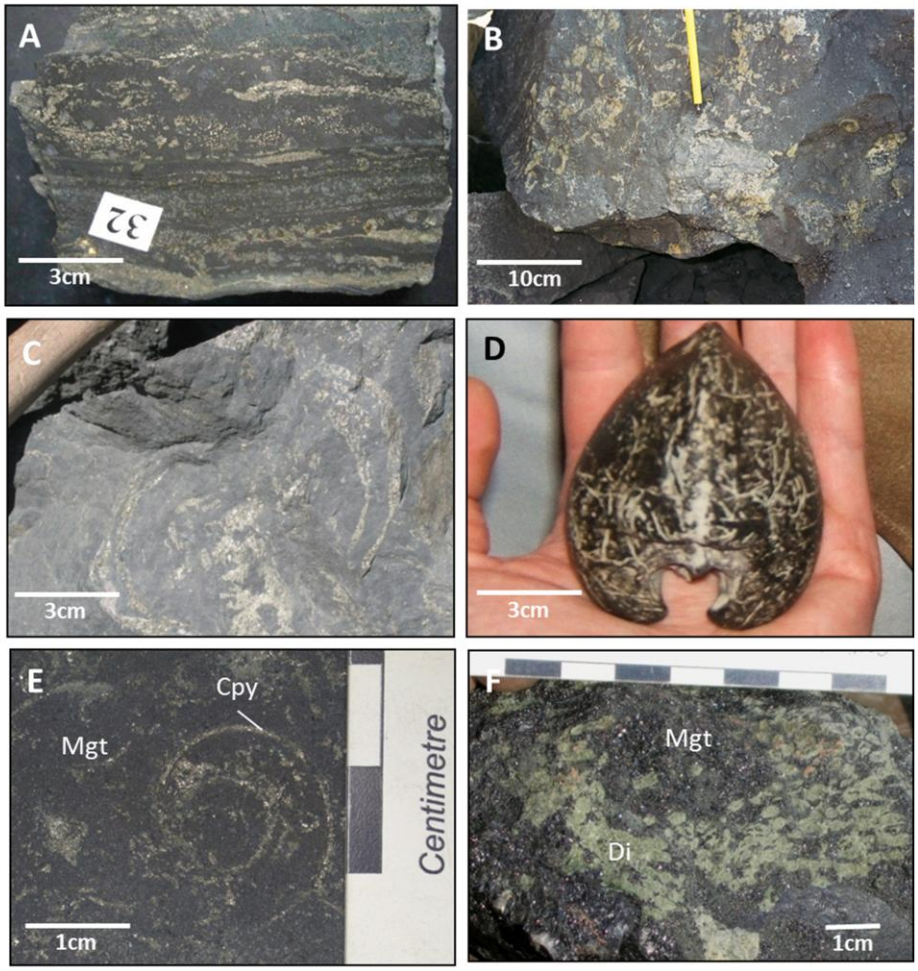

Figure 14

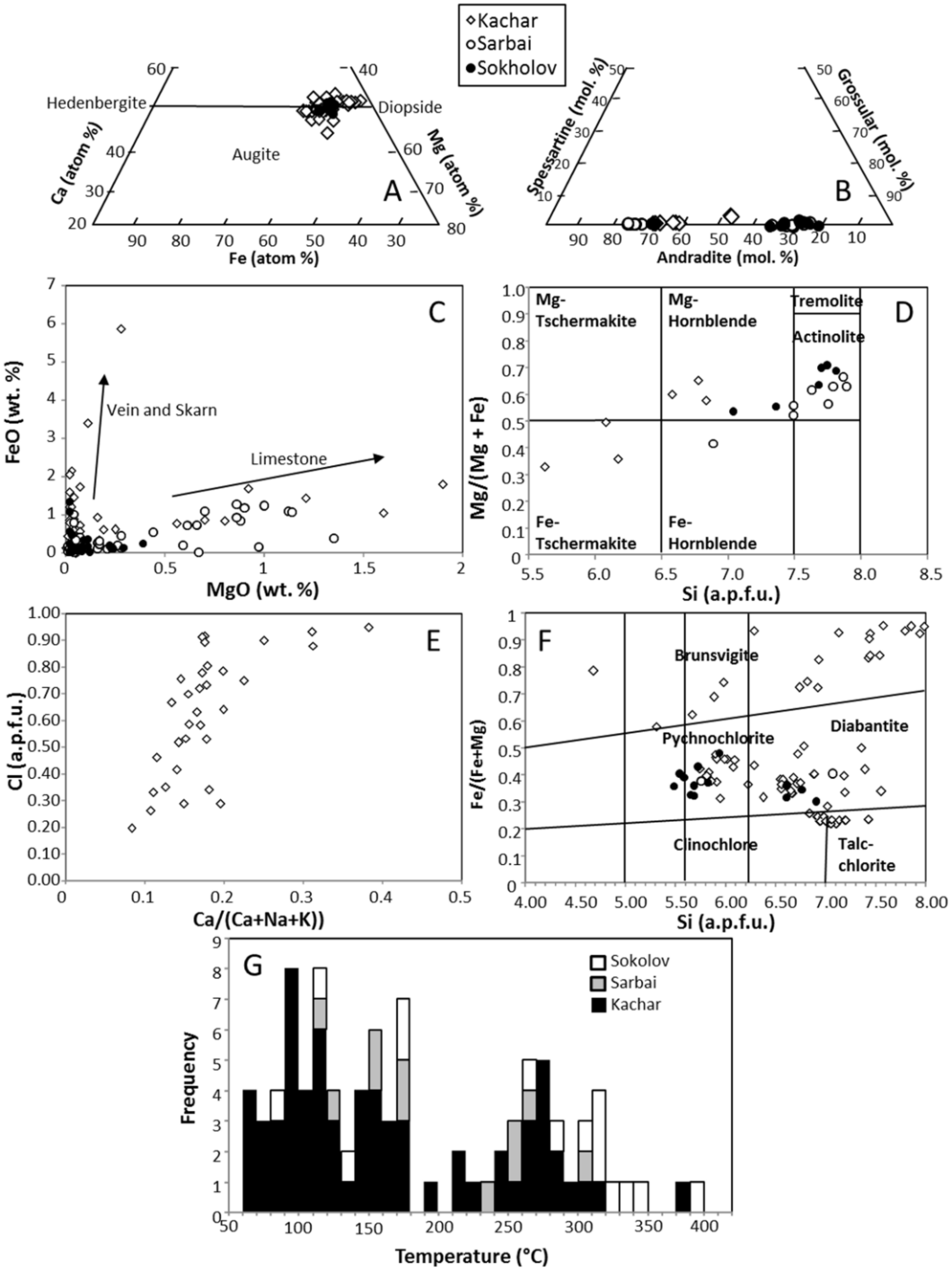

Figure 15

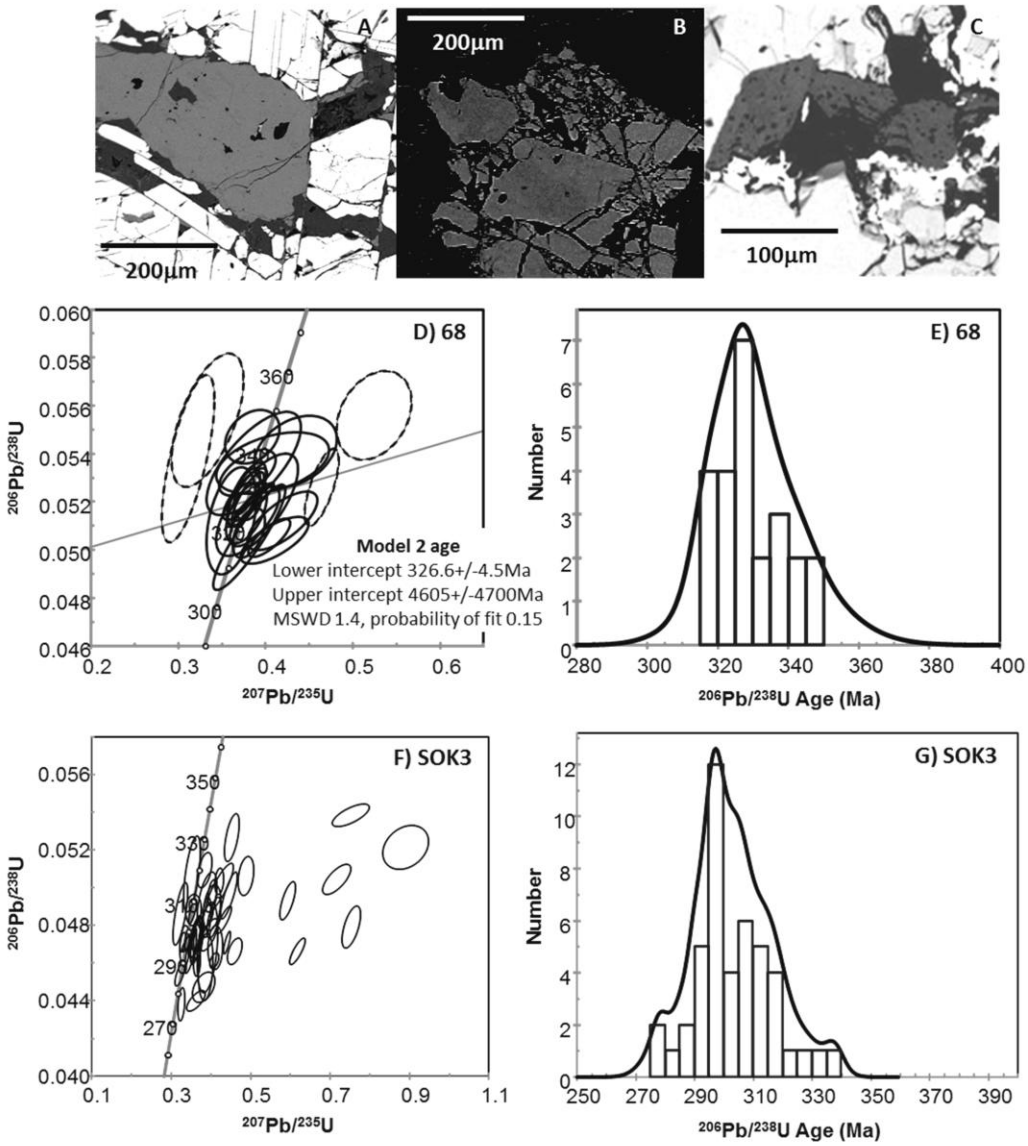

Figure 16

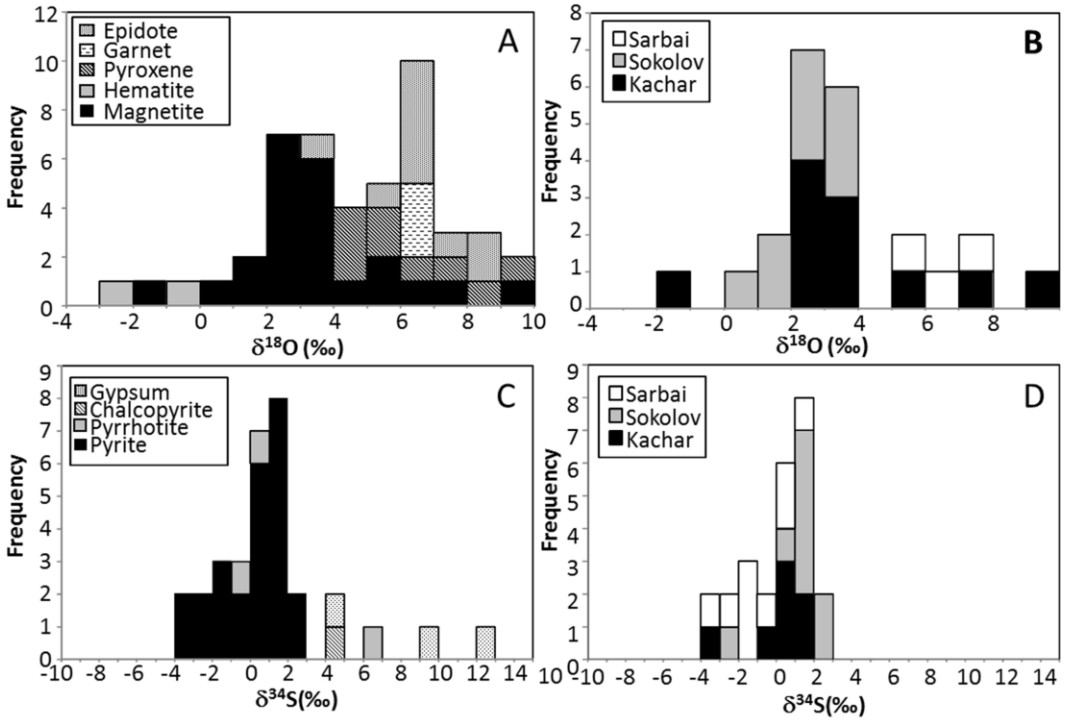

Figure 17

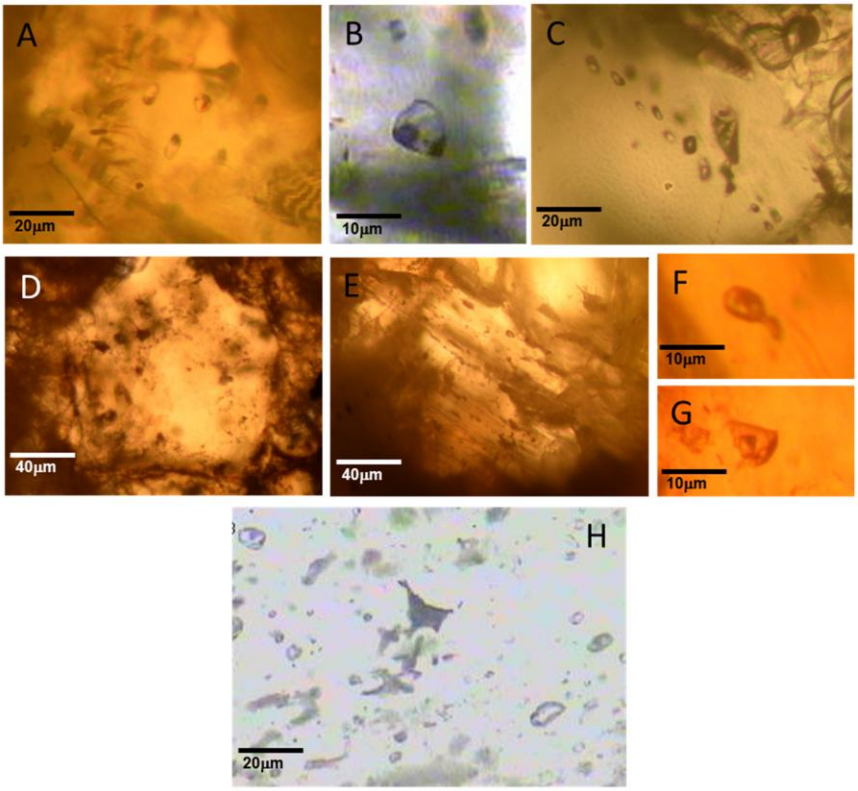

Figure 18

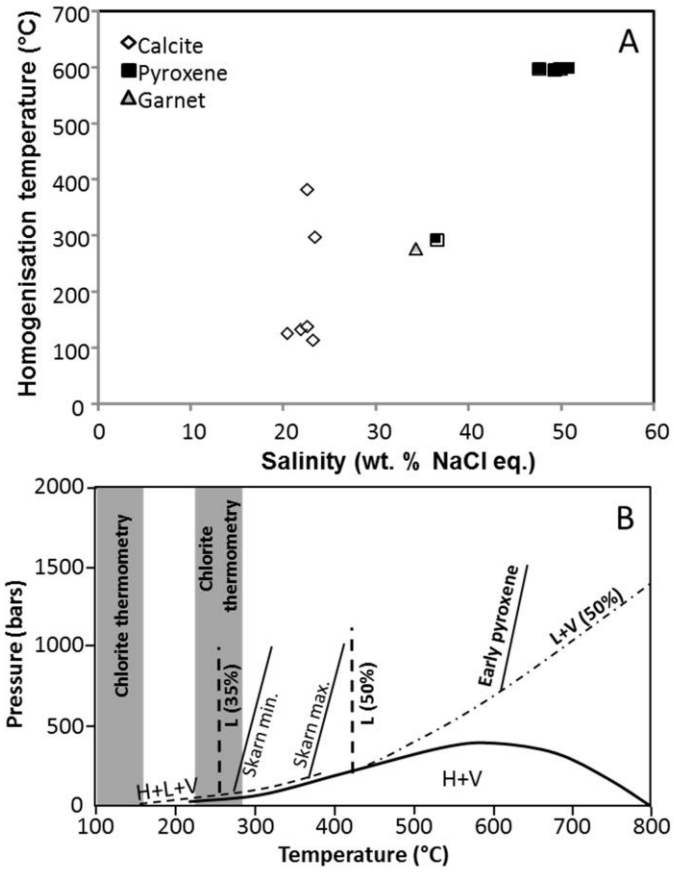

Figure 19

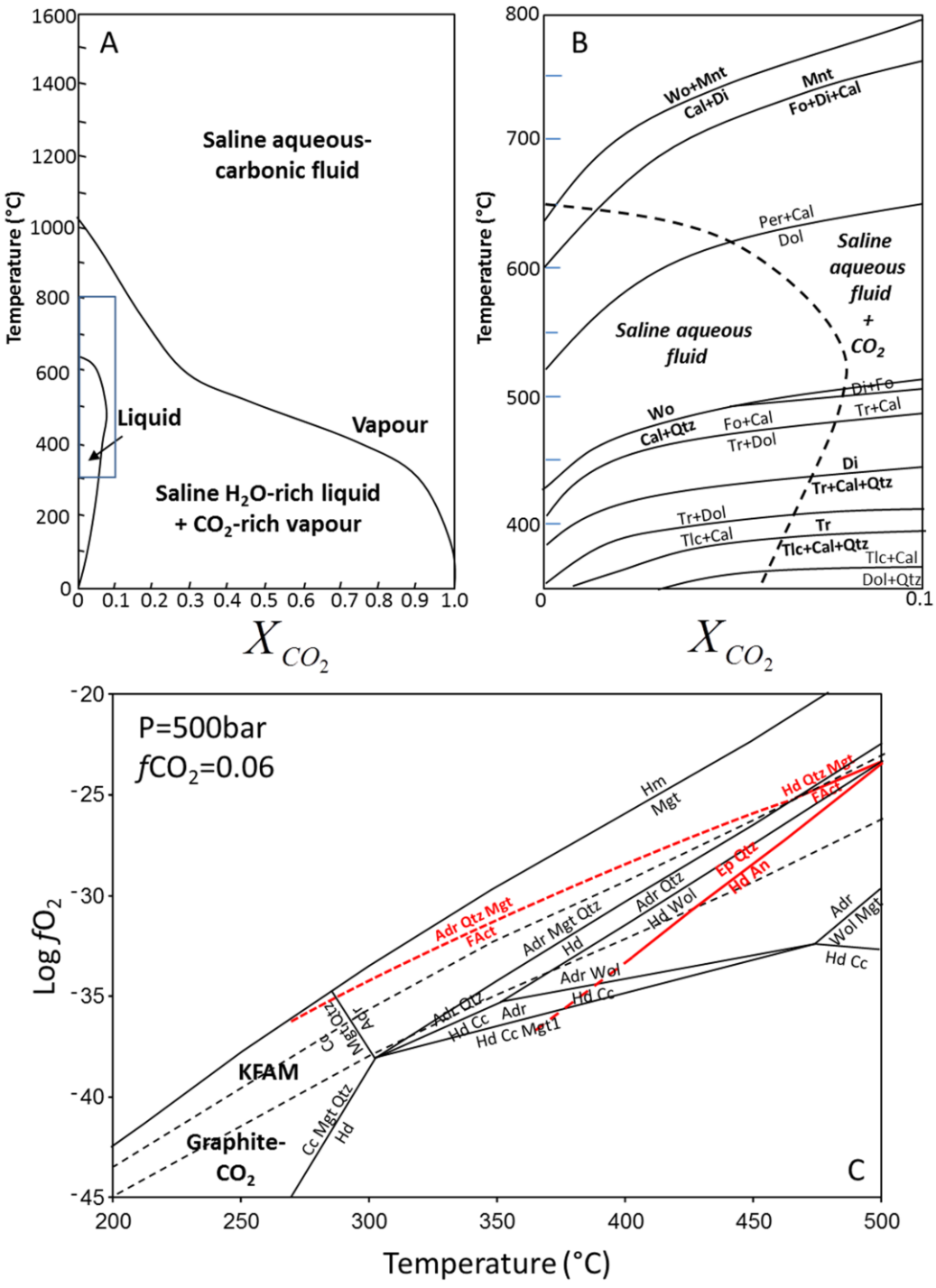

Figure 20

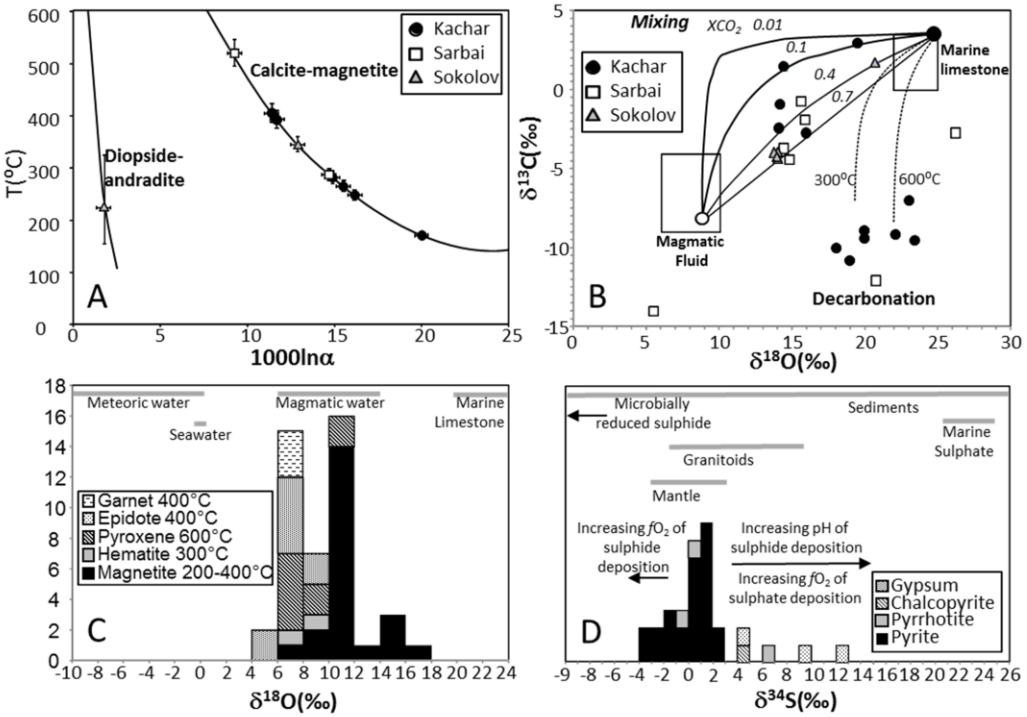

Figure 21

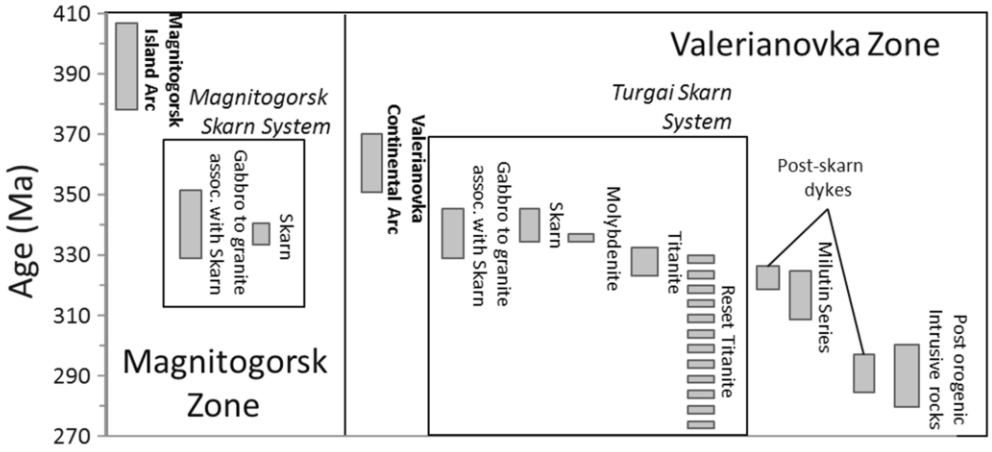

Figure 22

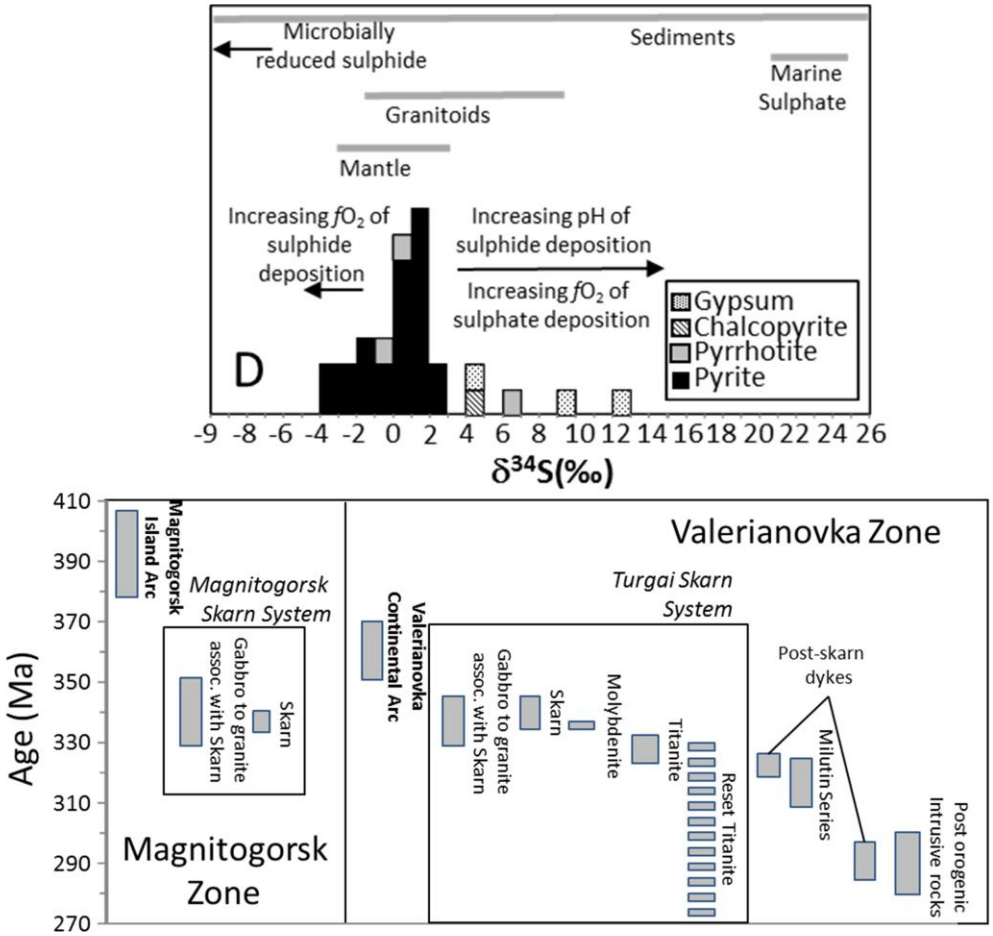

Graphical abstract

Highlights

- The Turgai deposits , Kazakhstan, host a resource of ~3 billion tonnes of iron ore.
- The deposits are unequivocally limestone replacement skarn bodies.
- They have affinities to Kiruna-type deposits (scapolite and albite alteration).
- The deposits were formed by igneous equilibrated fluids between ~600 and ~150°C.
- The age of skarns (336±1Ma) has implications for the closure of the Uralian ocean.